

Near-direct bandgap WSe_2/ReS_2 type-II pn heterojunction for enhanced ultrafast photodetection and high-performance photovoltaics

Abin Varghese,^{†, ‡, ¶} Dipankar Saha,[†] Kartikey Thakar,[†] Vishwas Jindal,[§]

Sayantana Ghosh,[†] Nikhil V Medhekar,[‡] Sandip Ghosh,[§] and Saurabh Lodha^{*, †}

[†]*Department of Electrical Engineering, Indian Institute of Technology Bombay, Mumbai 400076, India*

[‡]*Department of Materials Science and Engineering, Monash University, Clayton, Victoria 3800, Australia*

[¶]*IITB-Monash Research Academy, IIT Bombay, Mumbai 400076, India*

[§]*Department of Condensed Matter Physics and Materials Science, Tata Institute of Fundamental Research, Mumbai 400005, India*

E-mail: slodha@ee.iitb.ac.in

Abstract

PN heterojunctions comprising layered van der Waals (vdW) semiconductors have been used to demonstrate current rectifiers, photodetectors, and photovoltaic devices. However, a direct or near-direct bandgap at the heterointerface that can significantly enhance optical generation, for high light absorbing few/multi-layer vdW materials, has not yet been shown. In this work, for the first time, few-layer group-6 transition metal dichalcogenide (TMD) WSe_2 is shown to form a sizeable (0.7 eV) near-direct bandgap with type-II band alignment at its interface with the group-7 TMD ReS_2 through density functional theory calculations. Further, the type-II alignment and photogeneration across the interlayer bandgap have been experimentally confirmed through micro-photoluminescence and IR

photodetection measurements, respectively. High optical absorption in few-layer flakes, large conduction and valence band offsets for efficient electron-hole separation and stacking of light facing, direct bandgap ReS₂ on top of gate tunable WSe₂ are shown to result in excellent and tunable photodetection as well as photovoltaic performance through flake thickness dependent optoelectronic measurements. Few-layer flakes demonstrate ultrafast response time (5 μs) at high responsivity (3 A/W) and large photocurrent generation and responsivity enhancement at the heterostructure overlap region (10-100×) for 532 nm laser illumination. Large open circuit voltage of 0.64 V and short circuit current of 2.6 μA enables high output electrical power. Finally, long term air-stability and a facile single contact metal fabrication process makes the multi-functional few-layer WSe₂/ReS₂ heterostructure diode technologically promising for next-generation optoelectronic applications.

Introduction

Layered van der Waals (vdW) materials such as graphene, transition metal dichalcogenides (TMDs), and hBN are being studied for applications in photodetection,¹ terahertz spectroscopy,² photovoltaics,³ as well as flexible electronics.⁴ The ability to form epitaxy-free heterostructures by vertical stacking of these layered materials has enabled diverse material combinations and device applications.⁵⁻⁸ Specifically, heterostructures employing vdW semiconductors, with bandgaps in the visible and near-infrared wavelength range, have been used to demonstrate atomically thin pn junctions,^{1,6,9-14} light emitting diodes,⁹ photovoltaic cells,^{6,8,11,13} and memory devices.¹⁵ Although pn junctions using layered semiconductors have also been realized using electrostatic or chemical p and n doping in a single material (homojunctions),^{3,16} the approach of conjugating separate p- and n-type materials (heterojunctions) yields atomically abrupt junctions and exhibits efficient electron-hole separation owing to type-II band alignment as seen in WSe₂/MoS₂,^{6,9} BP/MoS₂,¹ MoTe₂/MoS₂,^{10,11} ReSe₂/ReS₂,^{12,13} GaTe/MoS₂¹⁴ heterostructures. However, a rational selection of the constituent p- and n-type semiconductors should be based on their intrinsic thickness dependent heterointerface electronic bandstructure, band alignment and optical properties, as well as extrinsic stability in the ambient and ability to form low resistance metal contacts. This can lead to the realization of technologically relevant pn junctions with excellent multi-functional (opto)electronic performance as demonstrated through WSe₂/ReS₂ gated pn heterostructures in this work.

Selection criteria for p and n materials

The semiconducting group-6 TMD WSe_2 , generally found in trigonal prismatic phase,¹⁷ is an indirect bandgap material in its bulk form.^{18,19} However, group-7 TMD e.g. 1T phase of ReS_2 is distorted octahedral in structure^{17,20} and exhibits direct (or, near-direct) bandgap at (or, close to) the Γ point of the Brillouin zone (BZ). Interestingly, unlike the group-6 TMDs, ReS_2 exhibits a unique property owing to its distorted structure and weak interlayer coupling- the direct or near-direct nature of its bandgap remains unchanged from monolayer to bulk.²⁰⁻²² Closer examination of the bandstructure of group-7 TMDs reveals that the conduction band minimum of ReS_2 remains at the Γ point, irrespective of the number of layers.^{20,23} But for group-6 TMDs (such as WSe_2) the valence band maximum relocates from K to Γ point of the BZ with increasing number of layers.^{18,24} It is important to note that the valence band maximum at the Γ point differs in energy only slightly from that at the K point.¹⁸ This gives rise to an increased probability of direct as well as indirect transitions from the Γ and the K valence maxima of WSe_2 to the Γ conduction minimum of ReS_2 respectively, for a predicted type-II band alignment. The possibility of a direct bandgap transition is not observed in a heterostructure of monolayer WSe_2 and monolayer/few-layer ReS_2 . Hence, interfacing few-layer (FL) flakes of group-6 WSe_2 and group-7 ReS_2 can significantly enhance internal quantum efficiency through increased heterointerface optical generation, a critical requirement for optoelectronic applications.

Higher photon absorption at the interfacial region of the heterostructure (overlap region) increases photogenerated carrier concentration leading to a larger external quantum efficiency that is essential for photovoltaic applications. Layered vdW materials have large absorption coefficients in the visible range for mono and few layers (nearly 10^5 cm^{-1} for 600 nm wavelength).²⁵ While the absorption is $\sim 10\%$ for monolayers,²⁶ it is significantly higher at $\sim 40\%$ for thicker flakes ($\sim 25 \text{ nm}$).²⁵ This makes FL ReS_2 a more appropriate choice for the top, light facing material in the $\text{WSe}_2/\text{ReS}_2$ pn heterostructure stack. Further, ultrathin FL TMDs of group-6 (here, WSe_2) show excellent modulation of the Fermi level with applied gate voltage,²⁷ in contrast to FL ReS_2 .²⁸ Controlled variation in the quasi-Fermi level difference between the p and n materials with gate bias can yield tunable open circuit voltages (V_{OC}).²⁹ Hence, FL WSe_2 is a more appropriate choice for the bottom, gate facing material in the $\text{WSe}_2/\text{ReS}_2$ pn heterostructure stack. Besides gate-tunable V_{OC} , in line with organic solar cells and also shown through atomistic simulations in this work, the large difference between the conduction band minimum of ReS_2 and the valence band maximum of WSe_2 is expected to result in a large V_{OC} value.^{10,30}

Previous studies have shown that Pt contacts on ReS_2 ³¹ and WSe_2 ²⁷ demonstrate n- an p-type transport, respectively. A single metal (Pt) for contacting both WSe_2 and ReS_2 requires a single lithography-metal deposition-liftoff process sequence. Several reports of pn heterojunctions with dissimilar metal electrodes for the p- and n-type layers (cf. Table 1) require additional fabrication steps. Further, WSe_2 and ReS_2 are both known to show long term stability in air without any capping layer.^{12,27} It is important to note that capping layers have been shown to enhance ambient stability in highly unstable materials such as black phosphorus. However, unlike electronic transport, capping layers can limit optoelectronic performance due to optical absorption losses. In summary, a combination of (i) high optical generation due to the near-direct bandgap at FL group-6/group-7 TMD interface, (ii) high optical absorption in thick TMD layers, (iii) direct bandgap of FL ReS_2 and high gate tunability of FL WSe_2 , (iv) single metal for p and n contacts, and, (v) air stability of uncapped WSe_2 and ReS_2 , can enable excellent optoelectronic performance and ease of fabrication in the type-II pn heterostructure, of a FL flake of ReS_2 (group-7) stacked on top of a gated FL flake of WSe_2 (group-6), as reported in this work.

Table 1 compares electrical, photodetection and photovoltaic parameters of published vdW pn heterostructures with the FL/FL $\text{WSe}_2/\text{ReS}_2$ heterostructure diode reported in this work, highlighting its versatile and superior optoelectronic performance. It demonstrates excellent pn diode action with a gate tunable current rectification ratio (RR) reaching 10^5 . High responsivity ($R = 3 \text{ A/W}$), large photo-amplification (10^6), a 10-to-100 times enhancement of photocurrent, and hence responsivity, at the heterostructure overlap region are consistent with the near-direct type-II band alignment at the heterointerface, calculated using density functional theory and confirmed through temperature and flake thickness dependent micro-photoluminescence (PL) measurements. Moreover, the interlayer bandgap allows infrared (IR) photodetection in energy range much lower than the bandgaps of the constituent WSe_2 and ReS_2 . The ultrafast photoswitching (rise (τ_r) and fall (τ_f) times of $\sim 5 \mu\text{s}$) shows efficient charge separation across the heterojunction and reinforces the predicted large type-II band offsets. Further, the large V_{oc} of 0.64 V is in close agreement with the calculated interlayer bandgap value of 0.7 V. Flake thickness dependent optoelectronic measurements justify the choice of FL flakes to achieve improved photodetection and photovoltaic metrics. Finally, long term photoswitching stability over months in ambient storage conditions, and a single contact metal process highlight the technological relevance of this work.

Table 1: Key electrical, photodetection and photovoltaic parameters of published vdW pn heterojunctions and the FL/FL WSe₂/ReS₂ heterostructure diode reported in this work

Ref.	p/n	M(p)- M(n)	G(p)- G(n)	Stable	Thickness	Electrical		Photodetection		Photovoltaic	
					(nm)	RR	η	R (A/W)	τ_r (ms)	V_{oc} (V)	I_{sc} (nA)
6	WSe ₂ /MoS ₂ *	Al-Pd	6-6	Yes	0.8/0.8	-	-	0.01	-	0.5	70
9	WSe ₂ /MoS ₂ *	Au	6-6	Yes	1.6/0.8	-	-	-	< 0.1	0.27	220
1	BP*/MoS ₂	Au	-6	No	11/0.8	10 ⁵	2.7	0.4	-	~ 0.3	~ 15
12	ReSe ₂ /ReS ₂ *	Pd	7-7	Yes	50.4/3.5	-	-	10 ⁵	4	-	-
10	MoTe ₂ */MoS ₂	Pt-Au	6-6	Yes	3/3	10 ³	1.3	0.3	25	0.3	200
29	GeSe/WSe ₂ *	Au	-6	Yes	52/6.5	10 ⁴	1.7	10 ³	-	0.7	3
32	GaSe*/InSe	Gr	-	No	19/13	10 ⁵	-	350	2 × 10 ⁻³	-	-
11	MoTe ₂ */MoS ₂	Pd-Au	6-6	Yes	3.3/7	80	-	0.3	0.06	0.51	1 × 10 ³
13	ReSe ₂ /ReS ₂ *	Pt-Ti	7-7	Yes	48/64	364	-	0.02	400	0.17	0.05
This work	WSe ₂ /ReS ₂ *	Pt	6-7	Yes	34/46	10 ³ - 10 ⁵	2	3	5 × 10 ⁻³	0.64	2.6 × 10 ³

G ~ TMD group, M ~ Metal, Gr ~ Graphene, η ~ ideality factor, * denotes the material on top

Atomistic Model

An atomistic study employing first-principles based density functional theory (DFT) calculations was carried out to gain insights into fundamental electronic properties of the WSe₂/ReS₂ vdW heterostructures. The DFT calculations were performed using the software package ‘QuantumATK’.^{33,34} To capture bulk intrinsic properties of the WSe₂/ReS₂ heterostructure, 4 layers (4L) of WSe₂³⁵ and 2 layers (2L) of distorted 1T-ReS₂³⁶ were considered (as illustrated in Figure 1a). The indirect bandgap of 4L WSe₂ was found to be 1.24 eV, whereas the direct bandgap of 2L ReS₂ was 1.40 eV (Figure 1b). Details of the calculations can be found in the ‘Methods’ section as well as in Supporting Information, S1. It should be noted that the bandgaps calculated for 4L WSe₂ and 2L ReS₂ are consistent with those of bulk WSe₂ and ReS₂.^{18,37,38} To further compare the calculated layer-dependent bandgap values of WSe₂ and ReS₂ with previously reported theoretical and experimental results, tables T1, T2 and figures S1.2, S1.3 have been included in the Supporting Information.

Calculated bandstructure in Figure 1b (i) depicts the conduction band minimum for 2L ReS₂ ($CB_{min,R}$) at the Γ point. Comparing this with monolayer DFT results (Supporting Information, Figure S1.1), it can be noticed that the $CB_{min,R}$ is near the Γ point irrespective of the number of layers.^{23,39} However, for WSe₂ the valence band maximum ($VB_{max,W}$) relocates from the K point to the Γ point of the BZ (Figure 1b (ii)), as the number of layers is increased from a monolayer to four layers. The $VB_{max,W}$ calculated at the Γ point is only 0.08 eV above than that at the K point. Such a trend in valence band dispersion has already been shown in previous studies.^{18,24} Figure 1c shows the computed

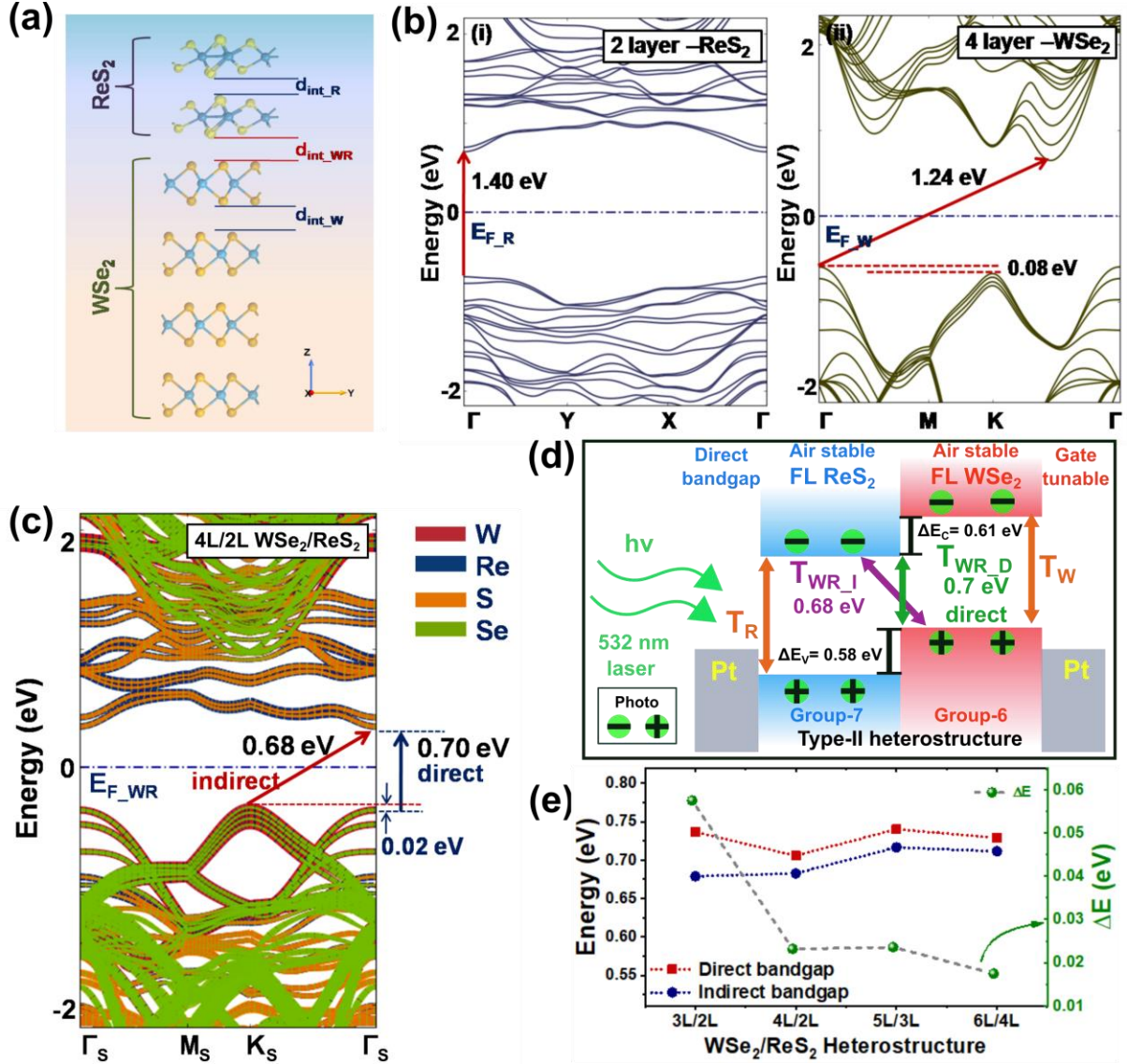


Figure 1: (a) Atomistic representation of 4L/2L WSe₂/ReS₂ vdW heterostructure, where d_{int_R} (~ 3.2 Å), d_{int_W} (~ 3.3 Å), and d_{int_WR} (~ 3.4 Å) are the optimized equilibrium distances. (b) Bandstructure of 2L ReS₂ and 4L WSe₂. (c) Projected bandstructure of 4L/2L WSe₂/ReS₂ vdW heterostructure showing element-wise contributions. E_{F_R} , E_{F_W} , and E_{F_WR} denote the Fermi level positions of 2L ReS₂, 4L WSe₂, and WSe₂/ReS₂ vdW heterostructure, respectively. The direct and indirect bandgap values are only 0.02 eV apart. (d) Schematic illustrating the near-direct type-II band alignment of the WSe₂/ReS₂ heterostructure. Here, the ΔE_C and ΔE_V values for the 4L/2L structure are 0.61 eV and 0.58 eV, respectively. The direct and indirect transition probabilities across the heterojunction are marked as T_{WR_D} and T_{WR_I} , respectively. T_W is the transition probability in WSe₂ and T_R in ReS₂. (e) Calculated direct and indirect bandgaps as well as the corresponding energy difference (ΔE) values of the various WSe₂/ReS₂ heterostructures.

bandstructure of the composite 4L/2L WSe₂/ReS₂ vdW heterostructure, along with the projections of element-wise contribution. Structural transformation of constituent materials into an optimized composite supercell gives rise to type-II band alignment with conduction band minimum at the Γ_S point and valence band maximum at the K_S point of the BZ. Moreover, the composite bandstructure is not just a superposition⁴⁰ of the bands originating from 2L ReS₂ (Figure 1b (i)) and 4L WSe₂ (Figure 1b (ii)), since it incorporates several quantum mechanical and structural effects like charge redistribution and percentage of strain on each material. The conduction band minimum due to ReS₂ forms a 0.68 eV indirect bandgap (Γ_S to K_S) with the valence band maximum contributed by WSe₂. However, the indirect bandgap is very close to the direct bandgap value (0.7 eV, at Γ_S). The possible optical transitions in the heterojunction are illustrated by double-headed arrows in Figure 1d, where the direct and indirect transition probabilities are represented by $T_{WR,D}$ (Γ_S to Γ_S) and $T_{WR,I}$ (K_S to Γ_S), respectively. It should be noted that for optical generation across the heterointerface, the direct bandgap transition $T_{WR,D}$ will not require phonon assisted momentum conservation, unlike $T_{WR,I}$. Hence, this near-direct⁴¹ electronic structure can lead to significantly large optical transitions at Γ_S which may contribute to enhanced photogeneration. This strongly correlates to the high responsivity obtained from the heterojunction in our focused laser measurements.

Furthermore, a closer look at Figure 1c shows a type-II bandstructure necessary for efficient separation of the photogenerated electrons and holes^{42,43} and can offer strong interlayer coupling via tunnelling of the majority carriers.^{6,42} This is further reinforced by strong photoluminescence quenching (Figure 3) and the region-wise photoresponse (Figure 5d) indicates maximum photoresponse at the WSe₂/ReS₂ interface region. Figure 1d also which illustrates a schematic representation of the projected bandstructure shown in Figure 1c, where the conduction and valence band offsets (ΔE_C and ΔE_V) are 0.61 eV and 0.58 eV, respectively. The near-direct interface bandgap (0.7 eV) enhances photogeneration and the large values of ΔE_C and ΔE_V favour easy and fast dissociation of the photogenerated electrons and holes thereby improving the photoresponsivity.^{6,42,43} The calculated sizeable bandgap value of 0.7 eV can also result in a relatively large V_{OC} .³⁰

To further investigate the band alignment in thicker WSe₂/ReS₂ heterostructures, atomistic models were designed using 5 layers of WSe₂ and 3 layers of ReS₂ (5L/3L WSe₂/ReS₂) and 6 layers of WSe₂ and 4 layers of ReS₂ (6L/4L WSe₂/ReS₂). Apart from that, a thinner 3L/2L WSe₂/ReS₂ heterostructure has also been considered for comparison. The electronic bandstructures for 3L/2L WSe₂/ReS₂, 5L/3L

WSe₂/ReS₂, and 6L/4L WSe₂/ReS₂ heterointerfaces are shown in Figure S1.3 of Supporting Information. The direct and indirect bandgaps as well as their energy difference (ΔE) for the thicker and thinner heterostructures are compared with the aforementioned 4L/2L case in Figure 1e. Although the thick (4L/2L and above) structures exhibit indirect bandgaps around 0.7 eV, their ΔE values always remain close to or less than 0.02 eV, rendering a near-direct nature⁴¹ to the bandstructure. Figure 1e justifies that the 4L/2L case can be used to represent the bandstructure of the thicker FL/FL WSe₂/ReS₂ heterostructure used for the optoelectronic measurements (described in the next section).

Results and Discussion

Device fabrication and physical characterization

FL WSe₂ and ReS₂ flakes were exfoliated from bulk crystals onto polydimethylsiloxane (PDMS) films. The WSe₂ flake was transferred first onto a 280 nm SiO₂/Si substrate. Next, the FL ReS₂ flake was aligned and transferred over WSe₂ ensuring a good overlap for the heterojunction. A schematic of the heterostructure showing the ReS₂ flake on top of WSe₂ is shown in Figure 2a. False colored scanning electron microscopy (SEM) image of the heterojunction is shown in Figure 2b and the contacts are labelled in the inset. An optical microscope image is available in Figure S2 of Supporting Information. Raman spectra from the individual materials as well as the overlap region are shown in Figure 2c. For FL ReS₂, Raman peaks at 161 and 212 cm⁻¹ are identified as the E_{2g} (in-plane) and A_{1g} (out-of-plane) vibration modes, respectively.²⁸ FL WSe₂ exhibits A_{1g} and 2LA(M) (second order Raman mode) peaks at 249 and 257 cm⁻¹ respectively.⁴⁴ Characteristic peaks corresponding to both materials are distinctly seen in the overlap region indicating good interface quality. Further, the thickness of each individual flake obtained by atomic force microscopy (AFM) is marked in the AFM image in Figure 2d. This device will be referred to as FL/FL WSe₂/ReS₂ heterostructure.

To examine the optical properties of the WSe₂/ReS₂ heterostructure, micro-PL studies were carried out using 532 nm laser with a spot diameter of $\sim 4 \mu\text{m}$. In addition to the aforementioned FL/FL structure, two samples with thinner constituents: (1) FL/8L WSe₂/ReS₂ (65 layers of WSe₂ and 8 layers of ReS₂) and (2) 2L/2L WSe₂/ReS₂ (Figure 3a) were studied (AFM data available in Supporting

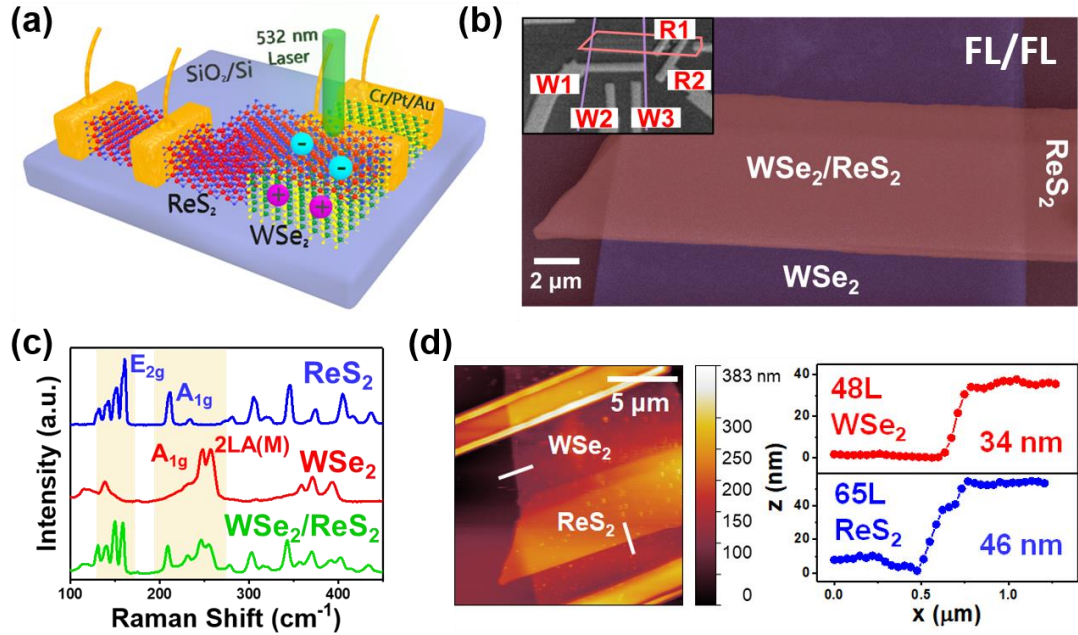


Figure 2: (a) Schematic of the $\text{WSe}_2/\text{ReS}_2$ heterostructure. (b) Scanning electron microscope image of the fabricated FL/FL heterostructure device. The bottom flake shown in blue is WSe_2 and ReS_2 , in red, is placed on top. The inset shows the contact labels. (c) Raman spectra acquired from individual WSe_2 and ReS_2 regions as well as from the overlap region showing characteristic peaks corresponding to both materials. (d) Atomic force microscope image of the FL/FL heterojunction area showing flake thicknesses.

Information, S3). The laser was selectively focused on the individual WSe_2 and ReS_2 regions as well as the $\text{WSe}_2/\text{ReS}_2$ overlap region. At 300 K, for the relatively thicker FL WSe_2 , in Figure 3b, the A and I peaks corresponding to the direct (K in conduction band to K in valence band) and indirect (between Γ and K in conduction band to Γ in valence band) transitions, respectively, and the direct bandgap peak (D) for 8L ReS_2 at Γ are prominent.^{18,20} The characteristic peaks from both materials are significantly quenched in the PL signal from the overlap region. For the thicker FL WSe_2 , the signal from the indirect bandgap is pronounced, hinting towards the increased possibility of transitions to the Γ of the BZ and in turn accumulation of photogenerated holes at Γ . The direct transitions in ReS_2 also occur at Γ . For the thinner 2L/2L $\text{WSe}_2/\text{ReS}_2$ heterostructure, at 300 K, the A and I peaks are merged, whereas at 25 K, the A peak shows a blueshift¹⁸ owing to the typical increase in the direct bandgap of a semiconductor with decrease in temperature. The PL from 2L layer ReS_2 was very weak

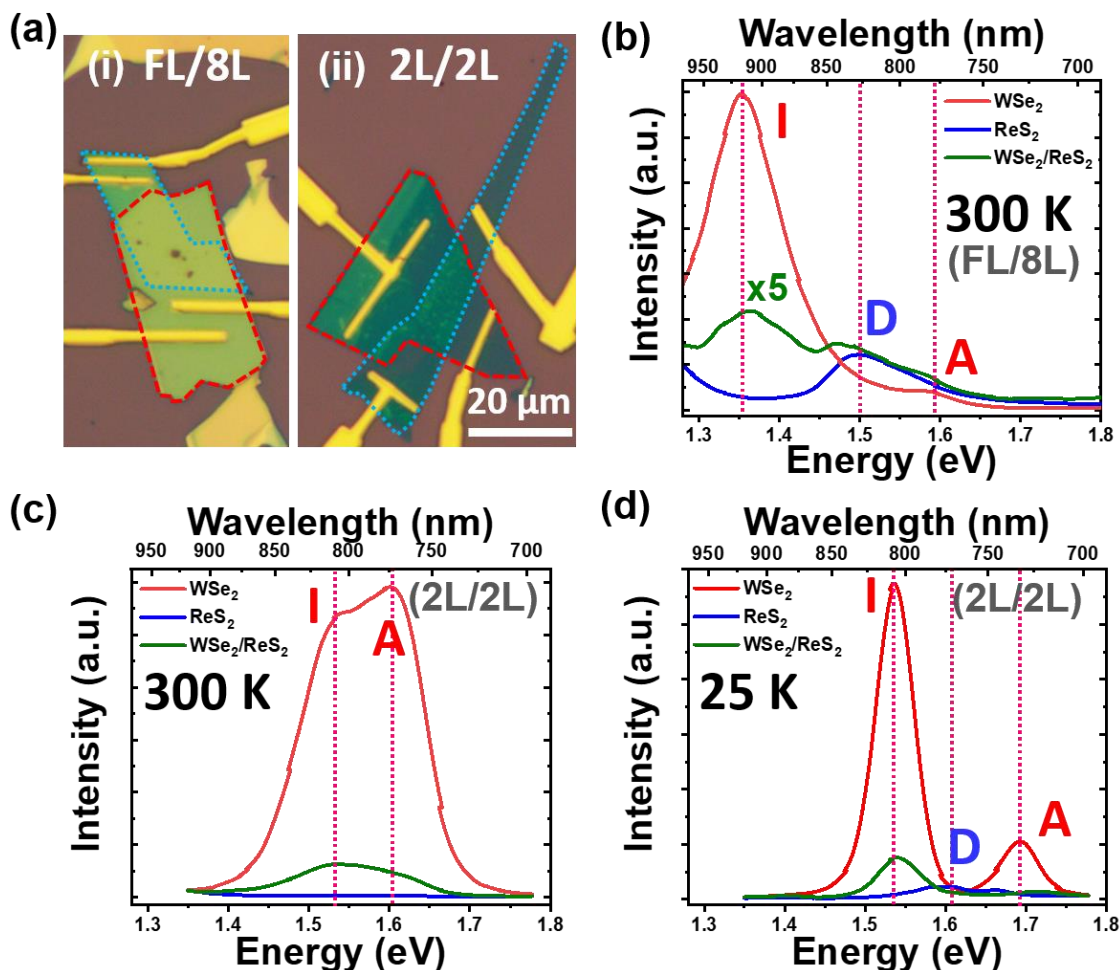


Figure 3: (a) Optical microscope images of (i) FL/8L and (ii) 2L/2L WSe₂/ReS₂ heterostructures. WSe₂ flakes are marked in red and ReS₂ in blue. (b) Room temperature PL signal from individual WSe₂ and ReS₂ regions as well as the WSe₂/ReS₂ overlap region of the FL/8L heterostructure showing considerable quenching of PL in the overlap region (multiplied by 5 for clarity). (c) Room temperature and (d) low temperature (25 K) PL data for 2L/2L heterostructure which also show PL quenching in the overlap region.

at room temperature and hence the measurement at 25 K was performed. In the 2L/2L heterostructure also, it was observed that the PL intensity was significantly reduced at the overlap region owing to efficient transfer of the laser induced photogenerated carriers across the heterojunction^{6,45} (electrons to ReS₂ and holes to WSe₂) indicating a type-II band alignment, in good agreement with the DFT predictions and consistent with many previous reports.^{6,45,46} The PL quenching data from a FL/FL heterostructure is available in S4 of Supporting Information. The absence of a PL signal due to recombination of interlayer excitons, if any, in the PL spectra captured

by the Si-based detector (detection range upto 1.1 eV) employed in this study reinforces the possibility of a lower energy (sub-1.1 eV) type-II interlayer bandgap.

Electrical characterization without illumination

For electrical characterization, multiple electrodes were fabricated on the heterostructures using electron beam lithography followed by sputtering of a Cr (< 5 nm)/Pt (50 nm)/Au (50 nm) metal stack. Pt has been reported to form ohmic contacts to ReS₂³¹ as well as WSe₂.²⁷ Individual field effect transistor (FET) performance was first analyzed using contacts only on WSe₂ (W2-W3) and only on ReS₂ (R1-R2). Transfer ($I_D - V_G$) and output ($I_D - V_D$) characteristics of these individual FETs are shown in Figure S5 of Supporting Information. For both FETs, the threshold voltage (V_{Th}) was obtained at the maximum transconductance (g_m) point in the transfer characteristics and the carrier mobility (μ) was calculated at V_{Th} using the equation: $\mu = \frac{L/W}{C_G V_D} \frac{dI_D}{dV_G}$. Here, L and W are the length and width of the channel, V_G and V_D are the gate and drain voltages, I_D is the drain current, and the oxide capacitance $C_G = 1.23 \times 10^{-8} \text{ Fcm}^{-2}$. The WSe₂ FET shows excellent modulation of I_D with V_G , demonstrating an on/off current ratio of 10^5 , with $V_{Th} = -28 \text{ V}$ and $\mu = 32 \text{ cm}^2 \text{ V}^{-1} \text{ s}^{-1}$. On the other hand, the ReS₂ FET shows a poor gate tunability of I_D and a lower $\mu = 3 \text{ cm}^2 \text{ V}^{-1} \text{ s}^{-1}$. FL ReS₂ flakes have been shown to exhibit very weak interlayer coupling²⁰ which could lead to reduced gate dependent charge carrier modulation in thicker flakes. Nevertheless, on/off current ratio of 10^8 is shown for a thinner (trilayer) ReS₂ FET in Figure S6 of Supporting Information. From the transfer characteristics of the individual FETs, n- and p-type characteristics are clearly observed for ReS₂ and WSe₂, respectively. Similar transport characteristics were observed for heterostructure devices without the Cr adhesion layer (S7 of Supporting Information). Further, the choice of WSe₂ as the bottom, gate facing, electrically tunable layer and FL direct bandgap ReS₂ as the top, light-facing, high optical absorption layer is justified.

The diode characteristics were measured across the contacts W1 on WSe₂ and R1 on ReS₂. V_G dependent output characteristics are shown in Figure 3a. WSe₂ was connected to the drain and ReS₂ to the source terminal. A maximum RR , defined as the ratio of the forward current (I_F) to the reverse current (I_R) at $V_D = \pm 1 \text{ V}$, of 6×10^3 was obtained at $V_G = -20 \text{ V}$. On comparing with the Shockley diode equation, $I_D = I_0 \left(\exp\left(\frac{qV_D}{\eta k_B T}\right) - 1 \right)$, where I_0 is the reverse leakage current, q is electronic charge, k_B is Boltzmann's constant, T is temperature, and η is ideality factor, the η is approximately 2 for various

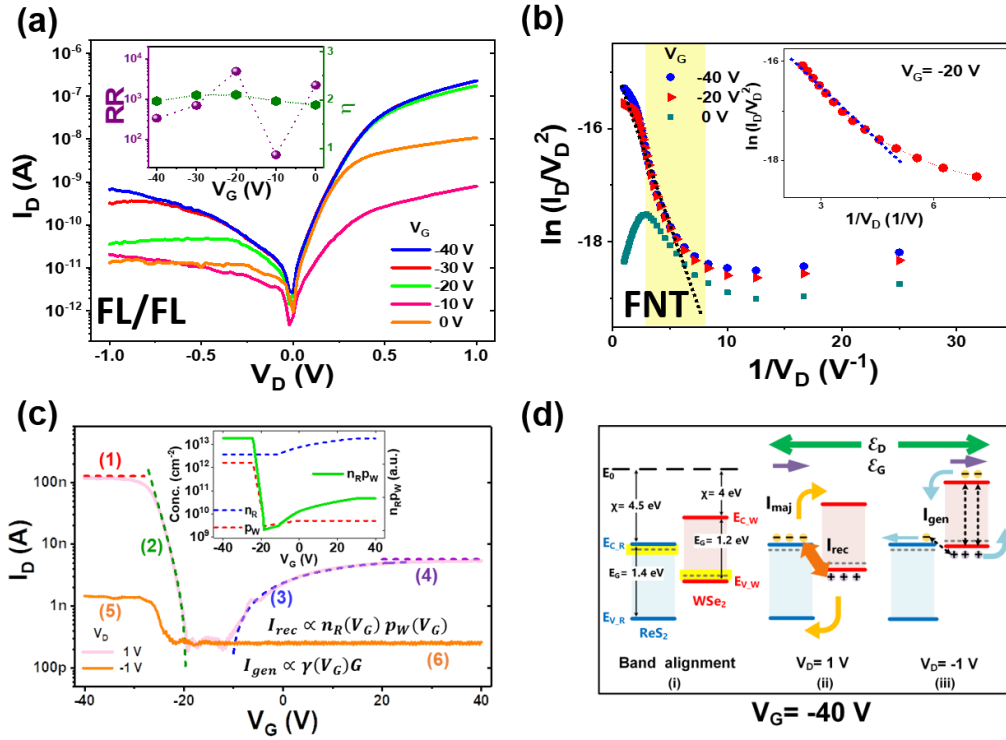


Figure 4: (a) Gate tunable output characteristics of the FL/FL WSe₂/ReS₂ pn heterojunction across the contacts W1 and R1. Inset shows the extracted values of rectification ratio and diode ideality factor as a function of applied back gate voltage. (b) Plot of $\ln(I_D/V_D^2)$ vs $1/V_D$ showing a linear region with a negative slope (inset) indicating Fowler-Nordheim tunneling transport through the heterostructure. (c) Transfer characteristics of the pn heterojunction for forward and reverse bias conditions with the various regions marked. Inset shows gate voltage dependent extracted hole sheet density in WSe₂ (p_W) and electron sheet density in ReS₂ (n_R) along with the product $n_R p_W$ that determines the interlayer recombination current. (d) Energy band diagrams for $V_G = -40$ V: (i) band alignment in WSe₂ and ReS₂ with their respective Fermi levels defined by the gate voltage, (ii) under forward bias, the dominant charge transport is governed by interlayer recombination of the majority carriers giving rise to I_{rec} , and (iii) for reverse bias the reduced current is due to intralayer and interlayer generation denoted by I_{gen} . \vec{E}_G and \vec{E}_D are the electric fields due to back gate and source-drain bias, respectively. The relative thickness of the arrows indicates the magnitude of the currents.

V_G , indicating recombination limited transport across the heterojunction. Figure S8 in the Supporting Information describes a similar device with RR reaching 10^5 . A significantly large series resistance (R_s) of the order of $M\Omega$ is extracted from the output characteristics at high V_D , which further increases at positive V_G due to reduced hole density in WSe₂. The output characteristics of the diode at positive V_G are shown in Figure S9 of Supporting Information.

In contrast to pn junctions fabricated using inorganic doped semiconductors like Si, the forward bias current transport in vdW pn heterojunctions is dominated by tunnelling-based trap assisted (Shockley-Read-Hall, SRH) or direct (Langevin) recombination of majority carriers across the heterointerface.^{6,47} The current transport due to Fowler-Nordheim tunnelling (FNT) through a triangular potential barrier is modelled by the equation:^{48,49} $I \propto V^2 \exp\left(\frac{-4d\sqrt{2m^*\phi^3}}{3\hbar qV}\right)$, where d is the thickness of the barrier, m^* is the effective mass of the charge carriers, \hbar is the reduced Planck's constant, and ϕ is the height of the tunnel barrier. Hence, the presence of tunnelling mediated transport can be confirmed by a straight line with negative slope in the $\ln(I_D/V_D^2)$ against $1/V_D$ plot. Figure 4b shows such a trend for forward bias V_D varying from 0.12 V to 0.4 V at different V_G . The triangular barrier required for FNT could be at the heterointerface or at the contacts. For $V_G < -20$ V, near the V_{Th} of WSe₂, I_F is high, implying WSe₂ dominated forward bias transport.

Transfer characteristics across the heterostructure are shown in Figure 4c for $V_D = 1$ V and $V_D = -1$ V. The forward bias transfer curve exhibits prominent n and p branches owing to contributions from both materials. The V_G dependent sheet carrier density of majority holes in WSe₂ is represented by p_W and majority electrons in ReS₂ by n_R . For V_G near the V_{Th} in WSe₂ and ReS₂ FETs, the I_D is approximated by the respective carrier concentrations (n) using the contact resistance (R_C) corrected drift current relation:^{50,51} $I_D = qn\mu(V_D - I_D R_C)(W/L)$. The p_W peaks at large negative V_G ($\sim 5.3 \times 10^{12}$ cm⁻²) and drops to its intrinsic value^{6,52} ($p_{W0} \sim 3 \times 10^9$ cm⁻²) below V_{Th} . On the other hand, n_R is extracted to be $\sim 1.8 \times 10^{13}$ cm⁻² at high positive V_G but it does not display considerable variation with V_G . Further, V_G dependent trends in the calculated values of n_R and p_W are shown in the inset of Figure 4c.

Being in close proximity to SiO₂, the Fermi level in thin WSe₂ can be effectively modulated by the gate bias. The electron affinities (χ) of WSe₂ and ReS₂ are considered to be 4 eV⁴⁸ and 4.5 eV,¹² respectively. Figure 4d (i) shows the energy band diagrams highlighting the positions of the Fermi levels in WSe₂ ($E_{F,W}$) and ReS₂ ($E_{F,R}$) for $V_G = -40$ V. Based on the transfer characteristics of the individual FETs, $E_{F,W}$ is assumed to be near the valence band and $E_{F,R}$ to be near the conduction band. When forward biased, a positive voltage is applied to WSe₂ and ReS₂ is kept grounded. Now, as described in Figure 4d (ii), for $V_G = -40$ V, there is an accumulation of majority charge carriers- electrons from ReS₂ and holes from WSe₂ at the heterointerface which can undergo interlayer recombination to yield a large current component, $I_{rec} \propto n_R p_W$, marked as region (1) in Figure 4c (n_R and p_W both being large). For the reverse bias case in Figure 4d (iii), since the direction of the source-drain electric field (\vec{E}_D) is now reversed, the current (marked as region (5) in Figure 4c) is due to generation of charge carriers in

WSe₂ (intralayer) or across the heterojunction (interlayer) and much smaller than the forward bias case. Further insights on the charge transport across the heterostructure for the various regions marked in Figure 4c and also at $V_G = 40$ V are provided in S10 of Supporting Information.

Photodetection

Optoelectronic characteristics of the three WSe₂/ReS₂ diode configurations (FL/FL, FL/8L, and 2L/2L) were studied using a 532 nm laser focused through a 50× objective yielding a spot of diameter ~ 4 μ m. The laser power (P_{laser}) was varied from 1 nW to 0.5 mW. Unless otherwise stated, all $I_D - V_D$ characteristics were recorded with an applied back gate voltage of -20 V for the FL/FL WSe₂/ReS₂ structure and -10 V for the two thinner configurations. For the FL/FL WSe₂/ReS₂ heterostructure, $I_D - V_D$ characteristics with increasing P_{laser} are shown in Figure 5a. The current under illumination is denoted by I_{light} , from which the photocurrent (I_{ph}) is calculated as $I_{ph} = I_{light} - I_{dark}$. I_{ph} depends on (i) generation of photoexcited electron-hole pairs (EHP) in the heterojunction region, (ii) efficient separation of the EHPs, and (iii) extraction of the carriers into the external circuit to contribute to the total current. Similar plots for the thinner heterostructures demonstrating lower photocurrents than the FL/FL diode for matched laser powers are shown in Figure S11 of Supporting Information. The high I_{ph} obtained in the FL/FL WSe₂/ReS₂ device can be attributed to (i) FL flakes for higher optical absorption, (ii) near-direct bandgap of the WSe₂/ReS₂ heterojunction for enhanced optical generation, and (iii) high values of ΔE_C and ΔE_V which lead to efficient charge separation across the heterointerface. Photo-amplification is the ratio of I_{light} to I_{dark} at different P_{laser} for a particular drain voltage. An enhanced photo-amplification exceeding 2×10^6 in the FL/FL WSe₂/ReS₂ heterostructure (Figure 5b) can enable excellent photodetection applications.

Responsivity ($R = I_{ph}/P_{laser}$) is a key figure of merit for photodetectors. A high R of 3 A/W at 1 nW of laser power, better than commercial Si photodetectors (for 532 nm)¹⁰ can be attributed to the large I_{ph} generated in the overlap region owing to the high absorption coefficients of the thick WSe₂ and ReS₂ flakes.⁵³ Consequently, the FL/8L and 2L/2L WSe₂/ReS₂ heterostructures demonstrate lower R that decreases with decreasing flake thicknesses. Absorption spectrum of a thick ReS₂ flake on sapphire substrate for small angle of incidence is shown in the Supporting Information, Figure S12. The variation of R with P_{laser} for the different heterostructures is shown in Figure 5c. A power

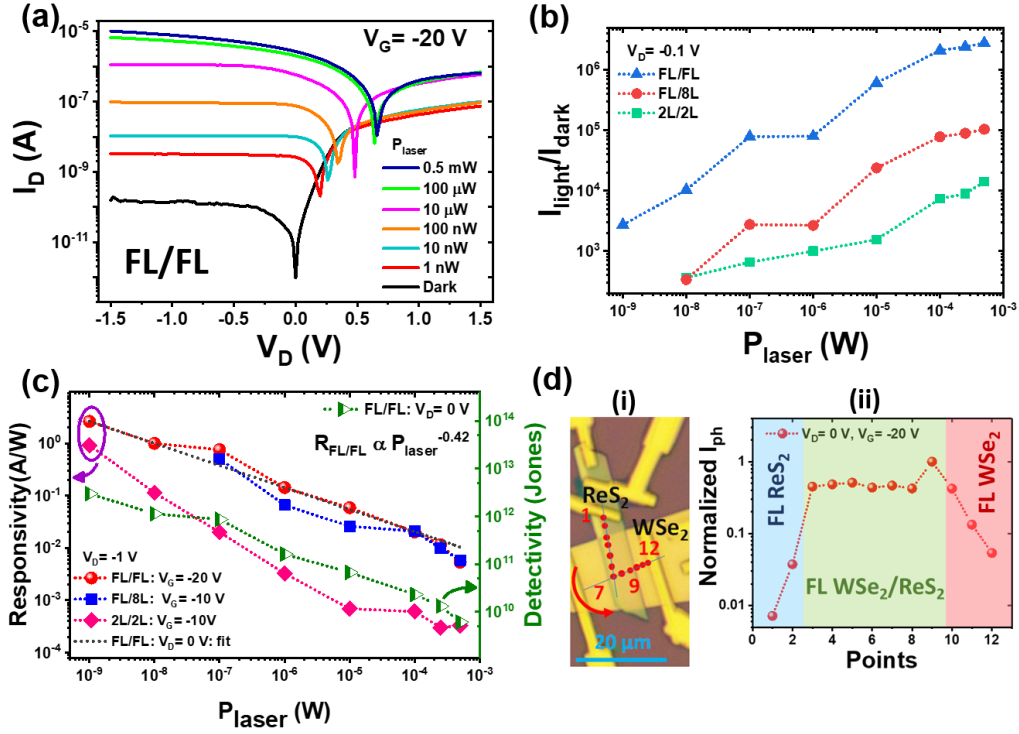


Figure 5: Photoresponse characteristics of $\text{WSe}_2/\text{ReS}_2$ heterojunctions. (a) $I-V$ characteristics under 532 nm laser illumination at various incident powers for FL/FL heterostructure. (b) Photo-amplification with laser power for $\text{WSe}_2/\text{ReS}_2$ heterojunctions having different thicknesses of constituent flakes at a low V_D of -0.1 V. (c) Responsivity for the different heterostructures, power law fit at $V_D = 0$ V, and detectivity (of FL/FL structure) at various laser powers. (d) Linescan showing region-dependent normalized photocurrent at $V_D = 0$ V, $V_G = -20$ V. The laser beam was converged to a spot size of $1 \mu\text{m}$ diameter and focused on the points marked in red in (i). The photoresponse from the different regions: only FL WSe_2 , FL/FL $\text{WSe}_2/\text{ReS}_2$ heterojunction, and only FL ReS_2 , is shown in (ii).

dependence of $R \propto P_{laser}^{-0.42}$ for $V_D = 0$ V is obtained by fitting the data. Detectivity (D^*) quantifies the photodetector's ability to measure very weak signals and can be calculated from the R and I_{dark} at a particular V_D and P_{laser} by the relation $D^* = \frac{R\sqrt{A}}{\sqrt{2qI_{dark}}}$. Here, A is the area of the device. A D^* value of 3×10^{12} Jones at $V_D = 0$ V and 1 nW illumination results in a noise equivalent power ($NEP = \frac{\sqrt{A}}{D^*}$) of 2×10^{-16} $\text{WHz}^{-1/2}$.

The variation of I_{ph} with V_G under reverse bias ($V_D = -1$ V) for the FL/FL heterostructure at 100 nW and 1 μW incident illumination is discussed in S13 of Supporting Information. As expected, the photocurrent increases with increasing illumination intensity and is significantly larger than the dark

transfer characteristics. I_{ph} vs V_G for the forward biased diode and the transport mechanisms are included in Figure S14 of Supporting Information. To map the origin of the photoresponse, the laser was selectively incident on multiple points (1 to 12) in three distinct regions of the FL/FL heterojunction: (1) ReS₂ only, (2) WSe₂/ReS₂ overlap and, (3) WSe₂ only, as marked in Figure 4f (i). Normalized I_{ph} for $V_D = 0$ V, $V_G = -20$ V is plotted in (ii) showing that the maximum current due to photogeneration is from the overlap region. In comparison to the individual WSe₂ and ReS₂ regions, the photocurrent shows 10-to-100 times increase in the overlap region, markedly higher than in BP/MoS₂,¹ WSe₂/SnS₂,⁵⁴ WSe₂/MoSe₂,⁵⁵ and MoS₂/GaSe⁵³ heterojunctions. This leads to a similar enhancement in R at the heterointerface in comparison to regions 1 and 3.

Photovoltaic effect and IR Photoresponse

A distinct photovoltaic effect is seen in the I - V characteristics in Figure 5a. Figure 6a shows the fourth quadrant (photovoltaic operating region) plot for increasing P_{laser} indicating the V_{OC} and I_{SC} . In organic solar cells the difference between the highest occupied molecular orbital (HOMO) of the donor and the lowest unoccupied molecular orbital (LUMO) of the acceptor limits the maximum V_{OC} .³⁰ Here, the difference between the conduction band minimum of FL ReS₂ and the valence band maximum of FL WSe₂ at the heterointerface (0.7 eV) being larger than several other reported vdW heterostructures, a relatively higher V_{OC} is predicted.^{10,30} As expected, for the FL/FL heterostructure, a high V_{OC} value of 0.64 V was obtained for $P_{laser} = 0.5$ mW. The corresponding I_{SC} was 2.6 μ A. Slope of the V_{OC} vs P_{laser} plot (described in Figure S15 of Supporting Information) gives an ideality factor of ~ 1.5 implying that both SRH and Langevin recombination processes influence the performance.

A modified Shockley diode equation⁵⁶: $I(V) = I_{ph} \left\{ \exp \left[\frac{q(V-V_{OC})}{k_B T (1+\alpha)} \right] - 1 \right\}$, is used to fit the I - V characteristics in the photovoltaic operation region. Here, α is a dimensionless quantity which depends on charge recombination and extraction.^{56,57} An α value of ~ 2 , for 10 nW and 100 nW laser illumination indicates good carrier extraction at the contacts. Fits to the I_D - V_D data for low illumination powers using the modified equation are shown in Figure 5b.

Power generated (P_{elec}) by the FL/FL photovoltaic device as a function of V_D for various illumination powers is shown in Figure 6c. The output power reaches 350 nW for $P_{laser} = 0.5$ mW, making it one of the highest values reported among vdW heterojunctions. The maximum electric power generated by the FL/8L and 2L/2L WSe₂/ReS₂ heterostructures, significantly (5 \times and 80 \times , respectively) lower

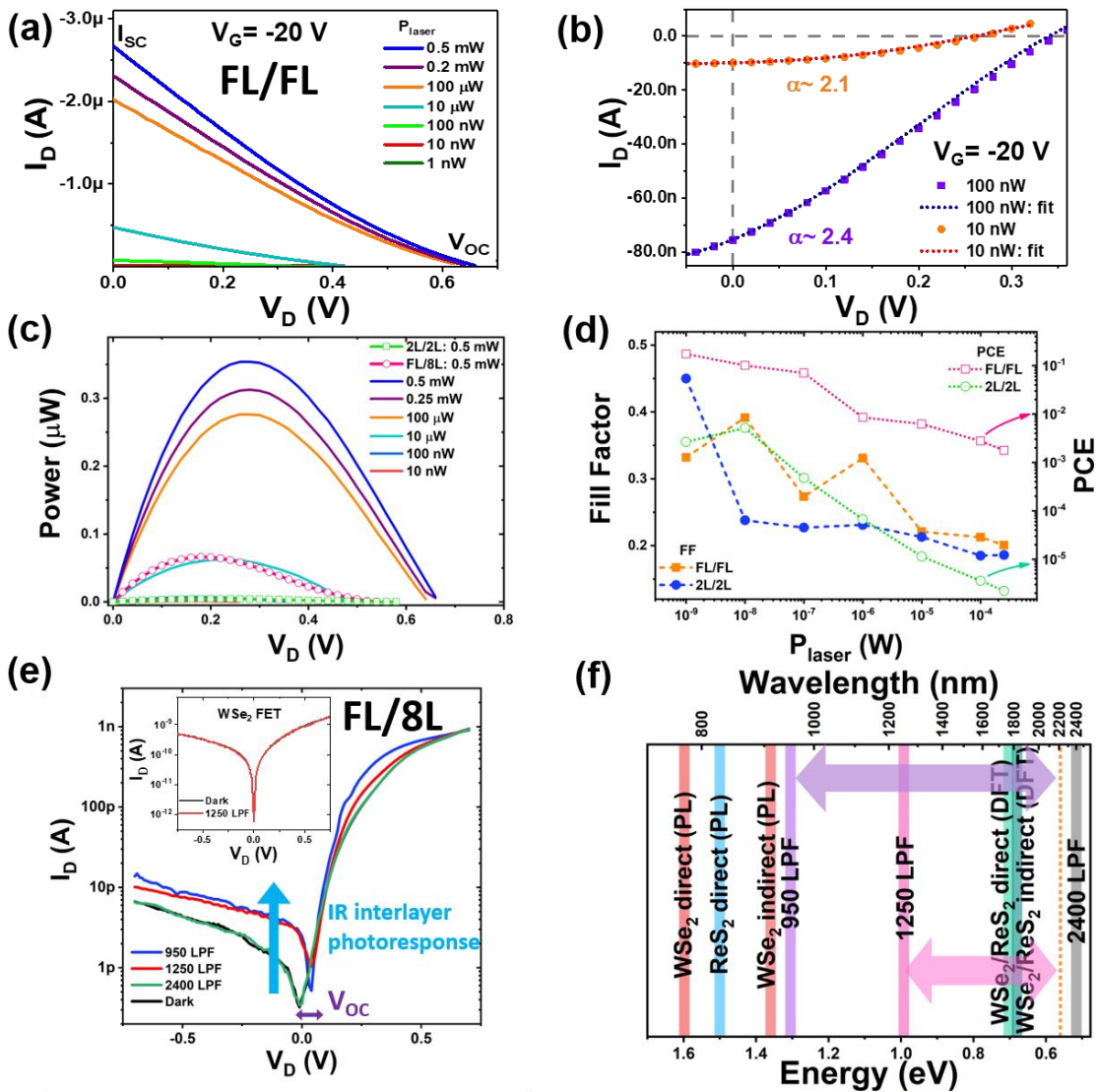


Figure 6: Photovoltaic effect and interlayer bandgap photoresponse in $\text{WSe}_2/\text{ReS}_2$ heterojunction. (a) Fourth quadrant plot showing I_{SC} and V_{OC} for varying laser power, and (b) fitting of photovoltaic data using the modified Shockley diode equation⁵⁶ for the FL/FL heterostructure. (c) Electrical power generated by the FL/FL device as a function of incident laser power. The maximum output electric power obtained for the FL/8L and 2L/2L heterostructures are also marked. (d) Fill factor and PCE at various laser powers for the FL/FL and 2L/2L heterostructures. (e) Output characteristics across the $\text{WSe}_2/\text{ReS}_2$ heterojunction under dark and upon IR illumination tuned using long pass filters. Photovoltaic effect and interlayer IR photoresponse are seen in the I-V characteristics. Inset shows that a WSe_2 FET does not have any response to the IR radiation above 1250 nm. (f) Plot depicting the energy range involved in the measurements.

than the FL/FL structure, is also shown in Figure 6c. Figure S16 of Supporting Information shows the variation in I_{SC} and V_{OC} with varying gate voltage and laser power. Similar to the transfer characteristics under illumination (S13 in Supporting Information), I_{SC} increases with laser power and is higher for negative gate voltages. V_{OC} is determined by the electron (ReS₂) and hole (WSe₂) quasi Fermi level difference upon illumination. In the FL/FL device, the Fermi level of ReS₂ stays near the conduction band and that of WSe₂ varies from the valence band edge upto midgap with back gate voltage. V_{OC} shows good tunability with V_G , with the maximum for $V_G \leq -30$ V when the Fermi levels of WSe₂ and ReS₂ are near their respective valence and conduction band edges, thereby maximizing $E_{Fn} - E_{Fp}$. Similarly, the minimum value for each incident power occurs for V_G below (more positive) V_{Th} of WSe₂. Further, the V_{OC} depends on the dark current as well as the light induced photocurrent in the pn junction. Owing to the reduced thickness and lower absorption coefficients of the constituent flakes in the thinner heterostructures, the V_{OC} is lower than the FL/FL structure as shown in Figure S17 of Supporting Information. As seen from Figure 6d, a maximum fill factor ($FF = P_{elec, max}/(V_{OC}I_{SC})$) of 0.4 and a maximum power conversion efficiency ($PCE = V_{OC}I_{SC}FF/P_{in}$) of 0.2 % are obtained. The FF and PCE of the thinner (2L/2L) heterostructure are compared to the thicker (FL/FL) device in Figure 6d. External quantum efficiency ($EQE = \frac{I_{ph}/q}{P_{laser}/h\nu} \times 100\%$) is ~ 600 % at 1 nW laser power. It should be noted that these values of EQE have been calculated from corresponding values of R ; the experimental values are typically found to be lower.²⁵

The strong PL quenching and enhanced photocurrent generation from the heterojunction overlap region are in good agreement with DFT calculations that predict a type-II band alignment at the heterointerface. The bandgaps of FL WSe₂ and ReS₂ are 1.35 eV and 1.50 eV as per our PL measurements (S4 of Supporting Information). The 532 nm (2.330 eV) laser excitation can lead to intralayer as well as interlayer generation of EHPs in the individual WSe₂ and ReS₂ layers and across the heterointerface, respectively. Therefore, to demonstrate photogeneration exclusively across the interlayer bandgap, the FL/8L heterostructure was irradiated using an IR source and various long pass filters (LPF) were used to selectively block wavelengths below the cut-on wavelength of the LPF. For instance, a 1250 LPF would only allow wavelengths beyond 1250 nm to pass through it. Figure 6e shows output characteristics of the diode under dark and on exposure to IR radiation tuned using three LPFs: 950 nm (1.305 eV), 1250nm (0.992 eV), and 2400 nm (0.516 eV). Photocurrent is obtained when 950 nm and 1250 nm LPFs are used, which correspond to energies significantly lower than the bandgaps of the individual materials and higher than the DFT predicted value for the interlayer bandgap. A clear photovoltaic effect is also seen in the $I - V$ characteristics. Furthermore,

the use of 2400 nm LPF yields negligible change from the dark characteristics. This observation rules out the contribution of sub-bandgap traps (if any) in the photocurrent generation across the interlayer bandgap.^{58,59} Absence of photoresponse in an individual WSe₂ FET (inset in Figure 6e) when subjected to IR radiation under the same set-up reinforces the sub-bandgap (type-II) interlayer photogeneration across the heterointerface. A schematic depicting the energy range involved in the optical measurements in comparison to the DFT interlayer bandgap values and the bandgaps of individual WSe₂ and ReS₂ layers is shown in Figure 6f for better visualization.

Photoswitching and Benchmarking

Transient photoresponse of the photodetector is a crucial measure for its use in high-speed applications. The three WSe₂/ReS₂ heterojunctions were exposed to laser illumination which was

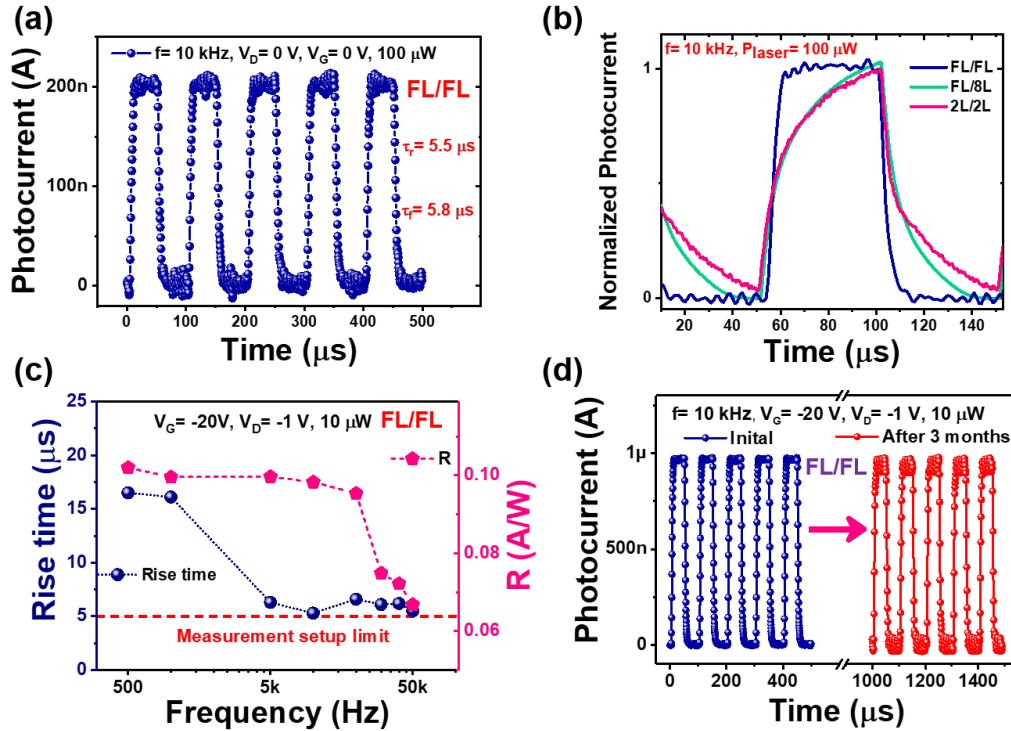


Figure 7: (a) Photoswitching at a frequency of 10 kHz with both V_G and V_D set at 0 V, showing self-powered operation for the FL/FL WSe₂/ReS₂ heterostructure. The rise and fall times are $\sim 5 \mu s$. (b) Normalized photocurrent demonstrating fast switching response at 10 kHz for heterostructures of different thicknesses. (c) Variation of rise time and responsivity of the FL/FL device with switching frequency of the laser at 10 μW power. (d) Photoswitching at 10 kHz and 10 μW laser power before and after three months of ambient exposure demonstrating air stability of the FL/FL heterostructure.

pulsed at frequencies ranging from 100 Hz to 50 kHz. The modulation of the photocurrent was recorded using a digital oscilloscope coupled to a low-noise amplifier. The rise time, τ_r (fall time, τ_f) is calculated between 10% (90%) to 90% (10%) of the photocurrent. Figure 7a shows the photocurrent for the FL/FL heterodiode under 100 μ W power switched at 10 kHz frequency, with both V_D and V_G kept at 0 V. This demonstrates the self-driven nature of the photodetection, owing to the photovoltaic effect, indicating good potential for ultra low-power applications. The τ_r and τ_f of $\sim 5 \mu$ s make the FL/FL structure one of the fastest reported vdW heterojunctions. Figure 7b compares

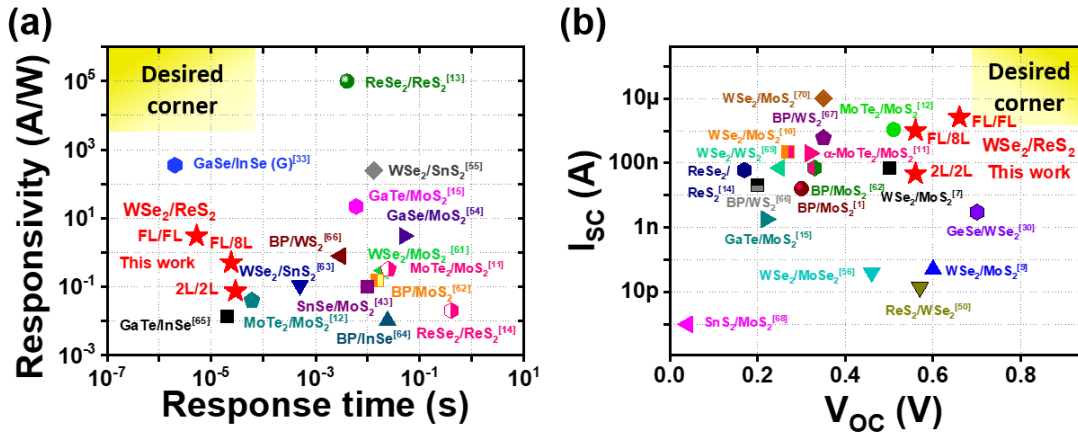


Figure 8: (a) Comparison of responsivity and response time of various vdW pn heterojunctions. This work demonstrates one of the fastest response times along with high responsivity. (b) Benchmarking of I_{sc} and V_{oc} of vdW pn heterojunctions with the current work showing excellent values of both parameters. R , τ_r , I_{sc} , and V_{oc} values for heterostructures of different thicknesses reported in this work are marked.

the photoswitching response of all three heterostructures at 10 kHz. The thinner heterostructures also exhibit fast switching, but slower than the FL/FL structure. The ultrafast response time can be partly attributed to the large band offsets (ΔE_C , ΔE_V) which enable prompt separation of the photogenerated charge carriers towards the contacts.⁶ Variation of τ_r and R with the switching frequency is shown in Figure 7c; indicating a possible trade-off between the two quantities as shown in other reports.²⁸ It may be noted that 5 μ s is the limit of the measurement setup used in this work. For the FL/8L and 2L/2L heterostructures, the response times are $\sim 24 \mu$ s and 28μ s, respectively. Stability is an essential parameter in the design space of vdW photodetectors since materials like BP, InSe are unstable⁶⁰ and can lead to degradation of device performance with time. Although capping layers can improve stability,⁶¹ they can also lead to optical absorption loss and a lower external quantum efficiency. The choice of individual p and n materials in this work was also based on their air-stability without the need of a capping layer. As expected, the heterostructure shows good

stability and a comparison of photoswitching response over a span of three months is shown in Figure 7d.

In order to benchmark the performance of our devices with published literature, a comparison of critical reported photodetector parameters, R and τ_r , are plotted in Figure 8a. Ideally, fast response time and high R are desirable for photodetection applications (top-left corner of the plot). The high value of R (3 A/W) and the ultrafast response time (5 μ s) of the FL/FL WSe₂/ReS₂ heterostructure indicate significantly better performance than previously reported vdW heterostructure photodetectors.^{10–12,29,32,42,54,62–67} To compare the photovoltaic performance, I_{sc} is plotted against V_{oc} for reported vdW heterostructures in Figure 8b. Excellent values of both, V_{oc} (0.64 V) and I_{sc} (2.6 μ A), are obtained for the current work in comparison to other reports.^{1,6,8,10,11,13,14,49,55,63,68–71}

Conclusions

This work demonstrates that an appropriate choice of n- and p-type materials from the group-6 and -7 TMDs can lead to excellent photodetection and photovoltaic performance. DFT calculations for the heterojunction composed of few-layer flakes of ReS₂ stacked onto WSe₂ predict type-II band alignment with a near-direct interlayer bandgap at the heterointerface which is experimentally supported by PL and IR photocurrent measurements. Excellent electrical characteristics are demonstrated with gate voltage tunable current rectification reaching 10^5 . Dark and illuminated diode transfer characteristics have been explained based on interlayer recombination and generation processes. In terms of photodetection, one of the fastest (5 μ s) high responsivity (3 A/W) transient photoswitching and the largest enhancement (10 - $100 \times$) in photocurrent generation and responsivity at the overlap region are reported for the WSe₂/ReS₂ pn heterostructure owing to the type-II near-direct bandgap, high optical absorption, and efficient charge carrier separation due to large heterointerface band offsets. High V_{oc} (0.64 V) resulting from gate tunability of WSe₂ and the 0.7 eV interlayer bandgap, large I_{sc} (2.6 μ A) and peak output power of 0.35 μ W make this one of the best reported heterostructure photovoltaic devices. Further, flake thickness dependent optoelectronic performance justifies the choice of FL flakes with high absorption coefficients. Finally, long term ambient stability and ease of fabrication due to a single contact metal process without capping layers, coupled with the multi-functional and excellent optoelectronic performance, makes the FL WSe₂/ReS₂ pn heterostructure significantly advance the prospects of 2D layered semiconductors enabling next-generation optoelectronic applications.

Methods

Computational Methodology

In order to carry out electronic structure calculations and geometry optimizations, density functional theory was employed using the generalized gradient approximation (GGA) exchange correlation in conjunction with the Perdew-Burke-Ernzerhof (PBE) functional.⁷² Moreover, as the norm-conserving pseudopotentials, the OPENMX (Open source package for Material eXplorer) code was used.^{73,74} For FL structures, $9 \times 9 \times 3$ k-points (in X, Y, and Z directions) along with the large density mesh cut off value of 200 Hartree were adopted. To account for the vdW interaction at different interfaces, the Grimme's dispersion correction (DFTD2) was utilized.⁷⁵

Device Fabrication and Characterization

The heterostructures were fabricated on an SiO_2 (285 nm)/ p^+ global back gate substrate. ReS_2 (HQ Graphene) and WSe_2 (SPI Supplies) were exfoliated onto PDMS stamps and selected flakes were transferred onto the substrate using a micromanipulator set-up. The heterostructure was cleaned in acetone to remove organic residues. The samples were spin coated with EL9/PMMA-A4 bilayer resist and electron beam lithography (Raith 150-Two) was followed by deposition of Cr (< 5 nm)/Pt (50 nm)/ Au (50 nm) stack (7-target sputtering system from AJA International) to define the contacts. Following metal lift-off in acetone, the heterostructure was annealed at 200 °C to remove resist residues. Raman measurements were carried out on LabRAM HR800 (HORIBA Scientific) with a 1 μm spot diameter using a 532 nm laser. AFM measurements were performed using MFP-3D (Asylum Research Inc.). For PL measurements, the samples were irradiated with a 532 nm frequency doubled Nd-YAG laser via a 50 \times objective. The emitted luminescence was collected using a 0.5 m focal length Triax550 monochromator and detected using a Si-charge coupled device detector. For low temperature measurements, the samples were cooled in a liquid He flow cryostat with optical access.

Electrical measurements were carried out using a probe station connected to a Keysight B1500A parameter analyzer. For the photocurrent study, the metal contact pads on the substrate were wire-bonded onto a custom-made PCB and mounted on a home-built measurement box fixed on the stage of an Olympus BX63 microscope. The radiation from a 532 nm diode laser was incident on the heterostructure through a 50 \times objective (spot diameter of $\sim 4 \mu\text{m}$). Keysight B1500A was used for electrical measurements under illumination. For the photoswitching measurements, the laser beam was directly modulated by applying pulses from 100 Hz to 50 kHz using a function generator (Agilent

33220A). The current from the device was fed to an SR570 low noise current pre-amplifier and its output was recorded on an Agilent DSO6012A digital storage oscilloscope.

Acknowledgement

A.V. thanks IITB-Monash Research Academy for the fellowship. D.S. acknowledges Department of Electrical Engineering, Indian Institute of Technology Bombay (IITB) for the Institute Post-Doctoral Fellowship. K.T. acknowledges Visvesvaraya PhD Scheme from the Ministry of Electronics and Information Technology (MeitY), Govt. of India. Authors acknowledge IITB Nanofabrication Facility (IITBNF) for usage of its facilities for device fabrication and characterization. N.V.M. acknowledges support from the Australian Research Council (CE170100039). This work was funded by the Department of Science and Technology, Govt. of India through the grant DST/SJF/ETA-01/2016-17. D.S. and K.T. contributed equally to the work.

Supporting Information Available

SI is included.

References

1. Deng, Y. X.; Luo, Z.; Conrad, N. J.; Liu, H.; Gong, Y. J.; Najmaei, S.; Ajayan, P. M.; Lou, J.; Xu, X. F.; Ye, P. D. Black Phosphorus-Monolayer MoS₂ van der Waals Heterojunction p-n Diode. *ACS Nano* **2014**, *8*, 8292–8299.
2. Low, T.; Avouris, P. Graphene plasmonics for terahertz to mid-infrared applications. *ACS Nano* **2014**, *8*, 1086–101.
3. Baugher, B. W.; Churchill, H. O.; Yang, Y.; Jarillo-Herrero, P. Optoelectronic devices based on electrically tunable p-n diodes in a monolayer dichalcogenide. *Nat. Nanotechnol.* **2014**, *9*, 262–7.
4. Akinwande, D.; Petrone, N.; Hone, J. Two-dimensional flexible nanoelectronics. *Nat. Commun.* **2014**, *5*, 5678.
5. Geim, A. K.; Grigorieva, I. V. van der Waals heterostructures. *Nature* **2013**, *499*, 419–25.
6. Lee, C. H.; Lee, G. H.; van der Zande, A. M.; Chen, W.; Li, Y.; Han, M.; Cui, X.; Arefe, G.; Nuckolls, C.; Heinz, T. F.; Guo, J.; Hone, J.; Kim, P. Atomically thin p-n junctions with van der Waals heterointerfaces. *Nat. Nanotechnol.* **2014**, *9*, 676–81.
7. Koppens, F. H.; Mueller, T.; Avouris, P.; Ferrari, A. C.; Vitiello, M. S.; Polini, M. Photodetectors based on graphene, other two-dimensional materials and hybrid systems. *Nat. Nanotechnol.* **2014**, *9*, 780–93.
8. Furchi, M. M.; Pospischil, A.; Libisch, F.; Burgdorfer, J.; Mueller, T. Photovoltaic effect in an electrically tunable van der Waals heterojunction. *Nano Lett.* **2014**, *14*, 4785–91.
9. Cheng, R.; Li, D. H.; Zhou, H. L.; Wang, C.; Yin, A. X.; Jiang, S.; Liu, Y.; Chen, Y.; Huang, Y.; Duan, X. F. Electroluminescence and Photocurrent Generation from Atomically Sharp WSe₂/MoS₂ Heterojunction p-n Diodes. *Nano Lett.* **2014**, *14*, 5590–5597.

10. Pezeshki, A.; Hossein, S.; Shokouh, H.; Nazari, T.; Oh, K.; Im, S. Electric and Photovoltaic Behavior of a Few-Layer α -MoTe₂/MoS₂ Dichalcogenide Heterojunction. *Adv. Mat.* **2016**, *28*, 3216–3222.
11. Chen, Y.; Wang, X.; Wu, G.; Wang, Z.; Fang, H.; Lin, T.; Sun, S.; Shen, H.; Hu, W.; Wang, J.; Sun, J.; Meng, X.; Chu, J. High-Performance Photovoltaic Detector Based on MoTe₂/MoS₂ van der Waals Heterostructure. *Small* **2018**, *14*, 1703293.
12. Jo, S.-H.; Lee, H. W.; Shim, J.; Heo, K.; Kim, M.; Song, Y. J.; Park, J.-H. Highly Efficient Infrared Photodetection in a Gate-Controllable van der Waals Heterojunction with Staggered Bandgap Alignment. *Adv. Sci.* **2018**, *5*, 1700423.
13. Cho, A.-J.; Namgung, S. D.; Kim, H.; Kwon, J.-Y. Electric and photovoltaic characteristics of a multi-layer ReS₂/ReSe₂ heterostructure. *APL Mat.* **2017**, *5*, 076101.
14. Wang, F.; Wang, Z. X.; Xu, K.; Wang, F. M.; Wang, Q. S.; Huang, Y.; Yin, L.; He, J. Tunable GaTe-MoS₂ van der Waals p-n Junctions with Novel Optoelectronic Performance. *Nano Lett.* **2015**, *15*, 7558–7566.
15. Wang, Q.; Wen, Y.; Cai, K.; Cheng, R.; Yin, L.; Zhang, Y.; Li, J.; Wang, Z.; Wang, F.; Wang, F.; Shifa, T. A.; Jiang, C.; Yang, H.; He, J. Nonvolatile infrared memory in MoS₂/PbS van der Waals heterostructures. *Sci. Adv.* **2018**, *4*, eaap7916.
16. Nipane, A.; Karmakar, D.; Kaushik, N.; Karande, S.; Lodha, S. Few-Layer MoS₂ p-Type Devices Enabled by Selective Doping Using Low Energy Phosphorus Implantation. *ACS Nano* **2016**, *10*, 2128–2137.
17. Chhowalla, M.; Shin, H. S.; Eda, G.; Li, L. J.; Loh, K. P.; Zhang, H. The chemistry of two-dimensional layered transition metal dichalcogenide nanosheets. *Nat. Chem.* **2013**, *5*, 263–275.
18. Zhao, W. J.; Ribeiro, R. M.; Toh, M. L.; Carvalho, A.; Kloc, C.; Neto, A. H. C.; Eda, G. Origin of Indirect Optical Transitions in Few-Layer MoS₂, WS₂, and WSe₂. *Nano Lett.* **2013**, *13*, 5627–5634.
19. Terrones, H.; Corro, E. D.; Feng, S.; Poumirol, J. M.; Rhodes, D.; Smirnov, D.; Pradhan, N. R.; Lin, Z.; Nguyen, M. A. T.; El'ias, A. L.; Mallouk, T. E.; Balicas, L.; Pimenta, M. A.; Terrones, M. New First Order Raman-active Modes in Few Layered Transition Metal Dichalcogenides. *Sci. Rep.* **2014**, *4*, 4215.
20. Tongay, S.; Sahin, H.; Ko, C.; Luce, A.; Fan, W.; Liu, K.; Zhou, J.; Huang, Y.-S.; Ho, C.-H.; Yan, J.; Ogletree, D. F.; Aloni, S.; Ji, J.; Li, S.; Li, J.; Peeters, F. M.; Wu, J. Monolayer behaviour in bulk ReS₂ due to electronic and vibrational decoupling. *Nat. Commun.* **2014**, *5*, 3252.
21. Chenet, D. A.; Aslan, O. B.; Huang, P. Y.; Fan, C.; van der Zande, A. M.; Heinz, T. F.; Hone, J. C. In-Plane Anisotropy in Mono- and Few-Layer ReS₂ Probed by Raman Spectroscopy and Scanning Transmission Electron Microscopy. *Nano Lett.* **2015**, *15*, 5667– 5672.
22. Lin, Y. C.; Komsa, H. P.; Yeh, C. H.; Bjorkman, T.; Liang, Z. Y.; Ho, C. H.; Huang, Y. S.; Chiu, P. W.; Krasheninnikov, A. V.; Suenaga, K. Single-Layer ReS₂: Two-Dimensional Semiconductor with Tunable In-Plane Anisotropy. *ACS Nano* **2015**, *9*, 11249–11257.
23. He, R.; Yan, J. A.; Yin, Z.; Ye, Z.; Ye, G.; Cheng, J.; Li, J.; Lui, C. H. Coupling and Stacking Order of ReS₂ Atomic Layers Revealed by Ultralow-Frequency Raman Spectroscopy. *Nano Lett.* **2016**, *16*, 1404–9.
24. Liu, G. B.; Xiao, D.; Yao, Y. G.; Xu, X. D.; Yao, W. Electronic structures and theoretical modelling of two-dimensional group-VIB transition metal dichalcogenides. *Chem. Soc. Rev.* **2015**, *44*, 2643–2663.
25. Jariwala, D.; Davoyan, A. R.; Wong, J.; Atwater, H. A. van der Waals Materials for Atomically-Thin Photovoltaics: Promise and Outlook. *ACS Photonics* **2017**, *4*, 2962– 2970.
26. Mukherjee, B.; Kaushik, N.; Tripathi, R. P. N.; Joseph, A. M.; Mohapatra, P. K.; Dhar, S.; Singh, B. P.; Kumar, G. V. P.; Simsek, E.; Lodha, S. Exciton Emission Intensity Modulation of Monolayer MoS₂ via Au Plasmon Coupling. *Sci. Rep.* **2017**, *7*, 41175.

27. Movva, H. C.; Rai, A.; Kang, S.; Kim, K.; Fallahazad, B.; Taniguchi, T.; Watanabe, K.; Tutuc, E.; Banerjee, S. K. High-Mobility Holes in Dual-Gated WSe₂ Field-Effect Transistors. *ACS Nano* **2015**, *9*, 10402–10.
28. Thakar, K.; Mukherjee, B.; Grover, S.; Kaushik, N.; Deshmukh, M.; Lodha, S. Multilayer ReS₂ Photodetectors with Gate Tunability for High Responsivity and High-Speed Applications. *ACS Appl. Mater. Interfaces* **2018**, *10*, 36512–36522.
29. Yang, Z. Y.; Liao, L.; Gong, F.; Wang, F.; Wang, Z.; Liu, X. Q.; Xiao, X. H.; Hu, W. D.; He, J.; Duan, X. F. WSe₂/GeSe heterojunction photodiode with giant gate tunability. *Nano Energy* **2018**, *49*, 103–108.
30. Elumalai, N. K.; Uddin, A. Open circuit voltage of organic solar cells: an in-depth review. *Energy Environ. Sci* **2016**, *9*, 391–410.
31. Park, J. Y.; Joe, H. E.; Yoon, H. S.; Yoo, S.; Kim, T.; Kang, K.; Min, B. K.; Jun, S. C. Contact Effect of ReS₂/Metal Interface. *ACS Appl. Mater. Interfaces* **2017**, *9*, 26325– 26332.
32. Yan, F. G.; Zhao, L. X.; Patane, A. L.; Hu, P. A.; Wei, X.; Luo, W. G.; Zhang, D.; Lv, Q. S.; Feng, Q.; Shen, C.; Chang, K.; Eaves, L.; Wang, K. Y. Fast, multicolor photodetection with graphene-contacted p-GaSe/n-InSe van der Waals heterostructures. *Nanotechnology* **2017**, *28*, 27LT01.
33. QuantumATK version 2018.06, Synopsys Quantumwise A/S, Available at <http://quantumwise.com/>.
34. Smidstrup, S.; Stradi, D.; Wellendorff, J.; Khomyakov, P. A.; Vej-Hansen, U. G.; Lee, M.E.; Ghosh, T.; Jónsson, E.; Jónsson, H.; Stokbro, K. First-principles Green's-function method for surface calculations: A pseudopotential localized basis set approach. *Phys. Rev. B: Condens. Matter Mater. Phys.* **2017**, *96*, 195309.
35. Schutte, W. J.; Deboer, J. L.; Jellinek, F. Crystal-Structures of Tungsten Disulfide and Diselenide. *J. Solid State Chem.* **1987**, *70*, 207–209.
36. Persson, K. Materials Data on ReS₂ (SG:2) by Materials Project.
37. Marzik, J. V.; Kershaw, R.; Dwight, K.; Wold, A. Photoelectronic Properties of ReS₂ and ReSe₂ Single-Crystals. *J. Solid State Chem.* **1984**, *51*, 170–175.
38. Kam, K. K.; Parkinson, B. A. Detailed photocurrent spectroscopy of the semiconducting group VIB transition metal dichalcogenides. *J. Phys. Chem.* **1982**, *86*, 463–467.
39. Liu, E.; Fu, Y.; Wang, Y.; Feng, Y.; Liu, H.; Wan, X.; Zhou, W.; Wang, B.; Shao, L.; Ho, C.-H.; Huang, Y.-S.; Cao, Z.; Wang, L.; Li, A.; Zeng, J.; Song, F.; Wang, X.; Shi, Y.; Yuan, H.; Hwang, H. Y. *et al.* Integrated digital inverters based on two-dimensional anisotropic ReS₂ field-effect transistors. *Nat. Commun.* **2015**, *6*, 6991.
40. Kosmider, K.; Fernandez-Rossier, J. Electronic properties of the MoS₂-WS₂ heterojunction. *Phys. Rev. B* **2013**, *87*, 075451.
41. Boztug, C.; Sanchez-Perez, J. R.; Yin, J.; Lagally, M. G.; Paiella, R. Grating-coupled mid-infrared light emission from tensilely strained germanium nanomembranes. *Appl. Phys. Lett.* **2013**, *103*, 201114.
42. Yang, S. X.; Wu, M. H.; Wang, B.; Zhao, L. D.; Huang, L.; Jiang, C. B.; Wei, S. H. Enhanced Electrical and Optoelectronic Characteristics of Few-Layer Type-II SnSe/MoS₂ van der Waals Heterojunctions. *ACS Appl. Mater. Interfaces* **2017**, *9*, 42149–42155.
43. Tongay, S.; Fan, W.; Kang, J.; Park, J.; Koldemir, U.; Suh, J.; Narang, D. S.; Liu, K.; Ji, J.; Li, J. B.; Sinclair, R.; Wu, J. Q. Tuning Interlayer Coupling in Large-Area Heterostructures with CVD-Grown MoS₂ and WS₂ Monolayers. *Nano Lett.* **2014**, *14*, 3185– 3190.
44. Zhao, W. J.; Ghorannevis, Z.; Amara, K. K.; Pang, J. R.; Toh, M.; Zhang, X.; Kloc, C.; Tan, P. H.; Eda, G. Lattice dynamics in mono- and few-layer sheets of WS₂ and WSe₂. *Nanoscale* **2013**, *5*, 9677–9683.
45. Hong, X.; Kim, J.; Shi, S.-F.; Zhang, Y.; Jin, C.; Sun, Y.; Tongay, S.; Wu, J.; Zhang, Y.; Wang, F. Ultrafast charge transfer in atomically thin MoS₂/WS₂ heterostructures. *Nat. Nanotechnol.* **2014**, *9*, 682.

46. Zhang, K.; Zhang, T.; Cheng, G.; Li, T.; Wang, S.; Wei, W.; Zhou, X.; Yu, W.; Sun, Y.; Wang, P.; Zhang, D.; Zeng, C.; Wang, X.; Hu, W.; Fan, H. J.; Shen, G.; Chen, X.; Duan, X.; Chang, K.; Dai, N. Interlayer Transition and Infrared Photodetection in Atomically Thin Type-II MoTe₂/MoS₂ van der Waals Heterostructures. *ACS Nano* **2016**, *10*, 3852–3858.
47. Roy, T.; Tosun, M.; Cao, X.; Fang, H.; Lien, D. H.; Zhao, P.; Chen, Y. Z.; Chueh, Y. L.; Guo, J.; Javey, A. Dual-gated MoS₂/WSe₂ van der Waals tunnel diodes and transistors. *ACS Nano* **2015**, *9*, 2071–9.
48. Doan, M. H.; Jin, Y.; Adhikari, S.; Lee, S.; Zhao, J.; Lim, S. C.; Lee, Y. H. Charge Transport in MoS₂/WSe₂ van der Waals Heterostructure with Tunable Inversion Layer. *ACS Nano* **2017**, *11*, 3832–3840.
49. Park, C.; Duong, N. T.; Bang, S.; Nguyen, D. A.; Oh, H. M.; Jeong, M. S. Photovoltaic effect in a few-layer ReS₂/WSe₂ heterostructure. *Nanoscale* **2018**, *10*, 20306–20312.
50. Fang, H.; Chuang, S.; Chang, T. C.; Takei, K.; Takahashi, T.; Javey, A. High Performance Single Layered WSe₂ p-FETs with Chemically Doped Contacts. *Nano Lett.* **2012**, *12*, 3788–3792.
51. Kaushik, N.; Nipane, A.; Basheer, F.; Dubey, S.; Grover, S.; Deshmukh, M. M.; Lodha, S. Schottky barrier heights for Au and Pd contacts to MoS₂. *Appl. Phys. Lett.* **2014**, *105*, 113505.
52. Paul, A. K.; Kuri, M.; Saha, D.; Chakraborty, B.; Mahapatra, S.; Sood, A. K.; Das, A. Photo-tunable transfer characteristics in MoTe₂/MoS₂ vertical heterostructure. *NPJ. 2D Mater. & Appl.* **2017**, *1*, 17.
53. Islam, A.; Lee, J.; Feng, P. X. L. Atomic Layer GaSe/MoS₂ van der Waals Heterostructure Photodiodes with Low Noise and Large Dynamic Range. *ACS Photonics* **2018**, *5*, 2693–2700.
54. Zhou, X.; Hu, X.; Zhou, S.; Song, H.; Zhang, Q.; Pi, L.; Li, L.; Li, H.; Lu, J.; Zhai, T. Tunneling Diode Based on WSe₂/SnS₂ Heterostructure Incorporating High Detectivity and Responsivity. *Adv. Mater.* **2018**, *30*, 1703286.
55. Flory, N.; Jain, A.; Bharadwaj, P.; Parzefall, M.; Taniguchi, T.; Watanabe, K.; Novotny, L. A WSe₂/MoSe₂ heterostructure photovoltaic device. *Appl. Phys. Lett.* **2015**, *107*, 123106.
56. Furchi, M. M.; Höller, F.; Dobusch, L.; Polyushkin, D. K.; Schuler, S.; Mueller, T. Device physics of van der Waals heterojunction solar cells. *NPJ. 2D Mater. & Appl.* **2018**, *2*, 3.
57. Wurfel, U.; Neher, D.; Spies, A.; Albrecht, S. Impact of charge transport on current voltage characteristics and power-conversion efficiency of organic solar cells. *Nat. Commun.* **2015**, *6*, 6951.
58. Xue, H.; Wang, Y.; Dai, Y.; Kim, W.; Jussila, H.; Qi, M.; Susoma, J.; Ren, Z.; Dai, Q.; Zhao, J.; Halonen, K.; Lipsanen, H.; Wang, X.; Gan, X.; Sun, Z. A MoSe₂/WSe₂ Heterojunction-Based Photodetector at Telecommunication Wavelengths. *Adv. Funct. Mater.* **2018**, *28*, 1804388.
59. Wang, G.; Li, L.; Fan, W.; Wang, R.; Zhou, S.; Lu, J.-T.; Gan, L.; Zhai, T. Interlayer Coupling Induced Infrared Response in WS₂/MoS₂ Heterostructures Enhanced by Surface Plasmon Resonance. *Adv. Funct. Mater.* **2018**, *28*, 1800339.
60. Goyal, N.; Kaushik, N.; Jawa, H.; Lodha, S. Enhanced stability and performance of few-layer black phosphorus transistors by electron beam irradiation. *Nanoscale* **2018**, *10*, 11616–11623.
61. Goyal, N.; Parihar, N.; Jawa, H.; Mahapatra, S.; Lodha, S. Accurate Threshold Voltage Reliability Evaluation of Thin Al₂O₃ Top-Gated Dielectric Black Phosphorous FETs Using Ultrafast Measurement Pulses. *ACS Appl. Mater. Interfaces* **2019**, *11*, 23673–23680.
62. Jeon, P. J.; Min, S. W.; Kim, J. S.; Raza, S. R. A.; Choi, K.; Lee, H. S.; Lee, Y. T.; Hwang, D. K.; Choi, H. J.; Im, S. Enhanced device performances of WSe₂-MoS₂ van der Waals junction p-n diode by fluoropolymer encapsulation. *J. Mater. Chem. C* **2015**, *3*, 2751–2758.
63. Ye, L.; Li, H.; Chen, Z. F.; Xu, J. B. Near-Infrared Photodetector Based on MoS₂/Black Phosphorus Heterojunction. *ACS Photonics* **2016**, *3*, 692–699.

64. Yang, T.; Zheng, B.; Wang, Z.; Xu, T.; Pan, C.; Zou, J.; Zhang, X.; Qi, Z.; Liu, H.; Feng, Y.; Hu, W.; Miao, F.; Sun, L.; Duan, X.; Pan, A. van der Waals epitaxial growth and optoelectronics of large-scale WSe₂/SnS₂ vertical bilayer p–n junctions. *Nat. Commun.* **2017**, *8*, 1906.
65. Zhao, S.; Wu, J.; Jin, K.; Ding, H.; Li, T.; Wu, C.; Pan, N.; Wang, X. Highly Polarized and Fast Photoresponse of Black Phosphorus-InSe Vertical p–n Heterojunctions. *Adv. Funct. Mater.* **2018**, *28*, 1802011.
66. Feng, W.; Jin, Z.; Yuan, J.; Zhang, J.; Jia, S.; Dong, L.; Yoon, J.; Zhou, L.; Vajtai, R.; Tour, J. M.; Ajayan, P. M.; Hu, P.; Lou, J. A fast and zero-biased photodetector based on GaTe-InSe vertical 2D p–n heterojunction. *2D Materials* **2018**, *5*, 025008.
67. Kwak, D.-H.; Ra, H.-S.; Jeong, M.-H.; Lee, A. Y.; Lee, J.-S. High-Performance Photovoltaic Effect with Electrically Balanced Charge Carriers in Black Phosphorus and WS₂ Heterojunction. *Adv. Mater. Interfaces* **2018**, *5*, 1800671.
68. Dastgeer, G.; Khan, M. F.; Nazir, G.; Afzal, A. M.; Aftab, S.; Naqvi, B. A.; Cha, J.; Min, K. A.; Jami, Y.; Jung, J.; Hong, S.; Eom, J. Temperature-Dependent and Gate Tunable Rectification in a Black Phosphorus/WS₂ van der Waals Heterojunction Diode. *ACS Appl. Mater. Interfaces* **2018**, *10*, 13150–13157.
69. Li, B.; Huang, L.; Zhong, M.; Li, Y.; Wang, Y.; Li, J.; Wei, Z. Direct Vapor Phase Growth and Optoelectronic Application of Large Band Offset SnS₂/MoS₂ Vertical Bilayer Heterostructures with High Lattice Mismatch. *Adv. Electron. Mater.* **2016**, *2*, 1600298.
70. Huo, N.; Yang, J.; Huang, L.; Wei, Z.; Li, S. S.; Wei, S. H.; Li, J. Tunable Polarity Behavior and Self-Driven Photoswitching in p-WSe₂/n-WS₂ Heterojunctions. *Small* **2015**, *11*, 5430–8.
71. Wong, J.; Jariwala, D.; Tagliabue, G.; Tat, K.; Davoyan, A. R.; Sherrott, M. C.; Atwater, H. A. High Photovoltaic Quantum Efficiency in Ultrathin van der Waals Heterostructures. *ACS Nano* **2017**, *11*, 7230–7240.
72. Perdew, J. P.; Burke, K.; Ernzerhof, M. Generalized gradient approximation made simple. *Phys. Rev. Lett.* **1996**, *77*, 3865–3868.
73. Ozaki, T. Variationally optimized atomic orbitals for large-scale electronic structures. *Phys. Rev. B* **2003**, *67*, 155108.
74. Ozaki, T.; Kino, H. Numerical atomic basis orbitals from H to Kr. *Phys. Rev. B* **2004**, *69*, 195113.
75. Grimme, S. Semiempirical GGA-type density functional constructed with a long-range dispersion correction. *J. Comput. Chem.* **2006**, *27*, 1787–1799.

Supporting Information

Near-direct bandgap WSe₂/ReS₂ type-II pn heterojunction for enhanced ultrafast photodetection and high-performance photovoltaics

Abin Varghese,^{1,2,3} Dipankar Saha,¹ Kartikey Thakar,¹ Vishwas Jindal,⁴ Sayantan Ghosh,¹ Nikhil Medhekar,² Sandip Ghosh,⁴ and Saurabh Lodha^{1*}

¹*Department of Electrical Engineering, Indian Institute of Technology Bombay, Mumbai 400076, India*

²*Department of Materials Science and Engineering, Monash University, Clayton, Victoria 3800, Australia*

³*IITB-Monash Research Academy, IIT Bombay, Mumbai 400076, India*

⁴*Department of Condensed Matter Physics and Materials Science, Tata Institute of Fundamental Research, Mumbai 400005, India*

E-mail: slodha@ee.iitb.ac.in

S1: Details of DFT calculations

DFT calculations were performed using the software package ‘QuantumATK’.¹ For the electronic structure calculations and geometry optimizations, the generalized gradient approximation (GGA) was used as an exchange correlation along with the Perdew-Burke-Ernzerhof (PBE) functional.² Apart from that, as the norm-conserving pseudopotentials, ‘‘Open source package for Material eXplorer’’ (OPENMX) code was employed.^{3,4} The basis set for W, Re, S, and Se atoms were taken as ‘s3p2d1’, ‘s3p2d1’, ‘s2p2d1’, and ‘s2p2d1’, respectively. The k-points in the Monkhorst-Pack grid were set as $9 \times 9 \times 1$ (in X, Y, and Z directions) for calculating electronic structure of the unit cells, whereas for few-layer (FL) structures $9 \times 9 \times 3$ k-points were adopted. Besides, the density mesh cut off was selected to a large value of 200 Hartree. Considering the FL structures, Grimme’s dispersion correction DFTD2 was used to apprehend the van der Waals (vdW) interaction at the different interfaces.⁵ Furthermore, to avoid any spurious interaction between periodic images, sufficient vacuum was incorporated along the perpendicular (Z) direction.

In order to optimize the geometries of the unit cells as well as FL $\text{WSe}_2/\text{ReS}_2$ heterostructures, the LBFGS (Limited-memory Broyden Fletcher Goldfarb Shanno) algorithm was utilized. Before performing these electronic structure calculations, the structures were optimized with a force tolerance value of $0.01 \text{ eV}/\text{\AA}$ (along with a stress tolerance of $0.001 \text{ eV}/\text{\AA}^3$).

Figure S1 shows (a, b) the fully relaxed unit cells and (c, d) the bandstructures of monolayer WSe_2 and ReS_2 . The optimized lattice constants for the triclinic ReS_2 unit cell were obtained as $a = 6.55 \text{ \AA}$, $b = 6.46 \text{ \AA}$, and $c = 12.77 \text{ \AA}$ (with $\alpha = 104.05^\circ$, $\beta = 91.76^\circ$, and $\gamma = 118.86^\circ$).^{6,7} For monolayer ReS_2 ,

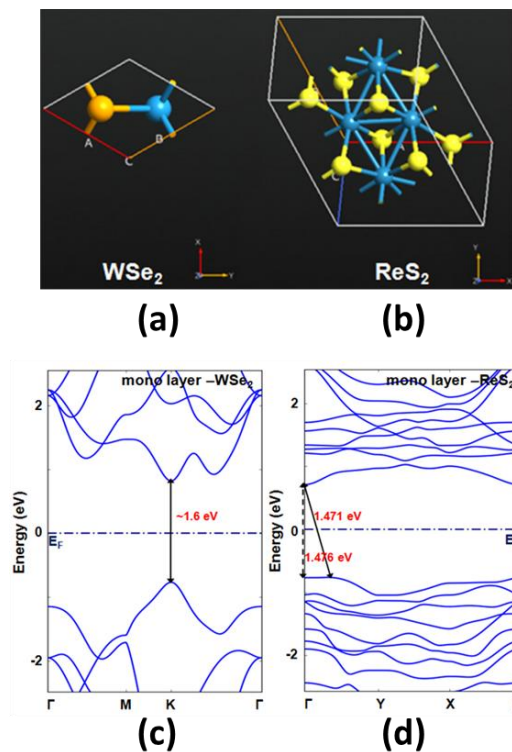


Figure S1.1: Geometry optimized unit cells of (a) WSe_2 and (b) ReS_2 , portrayed in the X-Y plane. Considering the X-Y plane view of the WSe_2 unit cell, it is important to note that the upper ‘Se’ atom is exactly on top of the lower one. Electronic bandstructures of monolayer WSe_2 and monolayer ReS_2 are shown in (c) and (d), respectively. E_F denotes the position of the Fermi level.

the direct band gap located at Γ point is ~ 1.476 eV. However, strictly speaking, the valence band maximum is not at Γ point (rather it lies in between Γ and Y points). Hence, monolayer ReS_2 exhibits a near-direct band gap of 1.471 eV. On the other hand, monolayer WSe_2 is a direct bandgap (~ 1.6 eV) semiconductor. The optimized lattice constants are $a = b = 3.32$ Å for the hexagonal WSe_2 unit cell.¹¹

Tables T1 and T2 illustrate the change in bandgaps with the increase in the number of layers of WSe_2 and ReS_2 , respectively. Layer dependent DFT calculated bandgaps and the ones obtained via photoluminescence (PL) are in good agreement with the corresponding literature.

WSe₂												
No. of layers	This Work			Bhattacharyya <i>et al.</i> ⁸			Kam <i>et al.</i> ⁹			Zhao <i>et al.</i> ¹⁰		
	Band gap (eV)	Method	Direct/ Indirect	Band gap (eV)	Method	Direct/ Indirect	Band gap (eV)	Method	Direct/ Indirect	Band gap (eV)	Method	Direct/ Indirect
1	1.59 1.65	Computational (GGA PBE + DFTD2) + Experimental	D	1.53	Computational (PBE + vdW)	D	--	Experimental	--	--	Experimental	--
2	1.46 1.53		I	1.43		I	--		--	1.53 (K- Γ)		I
3	1.32		I	--		--	--		--	1.45 (K- Γ) 1.42 (Λ - Γ)		I
4	1.24		I	--		--	--		--	1.42 (K- Γ) 1.37 (Λ - Γ)		I
5	1.21		I	--		--	--		--	--		--
6	1.18		I	--		--	--		--	--		--
8	1.16		I	--		--	--		--	1.37 (K- Γ) 1.28 (Λ - Γ)		I
10	1.15		I	--		--	--		--	--		--
FL	1.35		I	--		--	--		--	--		--
Bulk			--	1.08		I	1.20		I			--

Table T1: Comparison of the thickness dependent calculated (in green) bandgaps of WSe_2 with literature. The bandgaps obtained via photoluminescence (in red) measurements for flakes of different thickness are also compared with literature.

ReS ₂												
No. of layers	This Work			He <i>et al.</i> ¹²			Marzik <i>et al.</i> ¹³			Tongay <i>et al.</i> ¹⁴		
	Band gap (eV)	Method	Direct/Indirect	Band gap (eV)	Method	Direct/Indirect	Bandgap (eV)	Method	Direct/Indirect	Bandgap (eV)	Method	Direct/Indirect
1	1.476/ 1.471	Computational (GGA PBE + DFTD2) + Experimental	D/I	1.569/ 1.532	(LDA PZ)	D/I	---	Experimental		1.43 1.59	Computational (GGA PBE) + Experimental	D/I
				1.431/ 1.424	(GGA PBE)	D/I	---					
2	1.40 1.50		D	---	Computational		---			1.51		
3	1.37		D	---			---					
4	1.37		D	---			---			1.50		
FL	1.50		--	---								
Bulk	---		--	---					1.32	I		1.35

Table T2: Comparison of the thickness dependent calculated (in green) bandgaps of ReS₂ with literature. The bandgaps obtained via photoluminescence (in red) measurements for flakes of different thickness are also compared with literature.

Next, the atomistic models for various heterostructures were designed using the geometry optimized WSe₂ and ReS₂ unit cells. The composite heterointerfaces consist of m layers (mL) of WSe₂ and n layers (nL) of ReS₂ (where $m=3, 4, 5$, and 6 and $n=2, 3$, and 4) and are represented as mL/nL WSe₂/ReS₂. The direct and indirect bandgaps as well as the corresponding ΔE (energy difference between direct and indirect bandgap values) for 3L/2L WSe₂/ReS₂, 4L/2L WSe₂/ReS₂, 5L/3L WSe₂/ReS₂, and 6L/4L WSe₂/ReS₂ heterostructures are listed in Table T3. It can be observed that for 3L/2L WSe₂/ReS₂ heterostructure, difference between direct and indirect bandgaps is comparatively large (0.057 eV). Beyond 3L/2L WSe₂/ReS₂, as the number of layers of the constituent materials is increased, ΔE values remain close-to 0.02 eV. As ΔE did not change significantly in thicker heterostructures, the electronic properties of the 4L/2L WSe₂/ReS₂ heterointerface were emphasized in this work (Figure 1).

For the composite 4L/2L WSe₂/ReS₂ heterointerface, the mean absolute strain on 4 layer-WSe₂ (as well as on 2 layer-ReS₂) was restricted to a small value of 0.66%. Besides, the stacking patterns for 4 layer-WSe₂ and 2 layer-ReS₂ were found to be in good agreement with previous studies.^{8,12} Next, the heterointerface was wrapped into a hexagonal supercell and fully relaxed with the aforementioned

force and stress tolerance values to construct the final structure. The optimized lattice constants for the 4L/2L WSe₂/ReS₂ vdW heterostructure are a= b= 6.621 Å.

WSe ₂ /ReS ₂ heterostructure	3L/2L	4L/2L	5L/3L	6L/4L
Direct bandgap (eV)	0.7365	0.7059	0.7402	0.7290
Indirect bandgap (eV)	0.6790	0.6827	0.7166	0.7115
ΔE (eV)	0.0575	0.0232	0.0236	0.0175

Table T3: Calculated direct and indirect bandgap values along with their corresponding difference (ΔE) for various FL WSe₂/ReS₂ heterostructures.

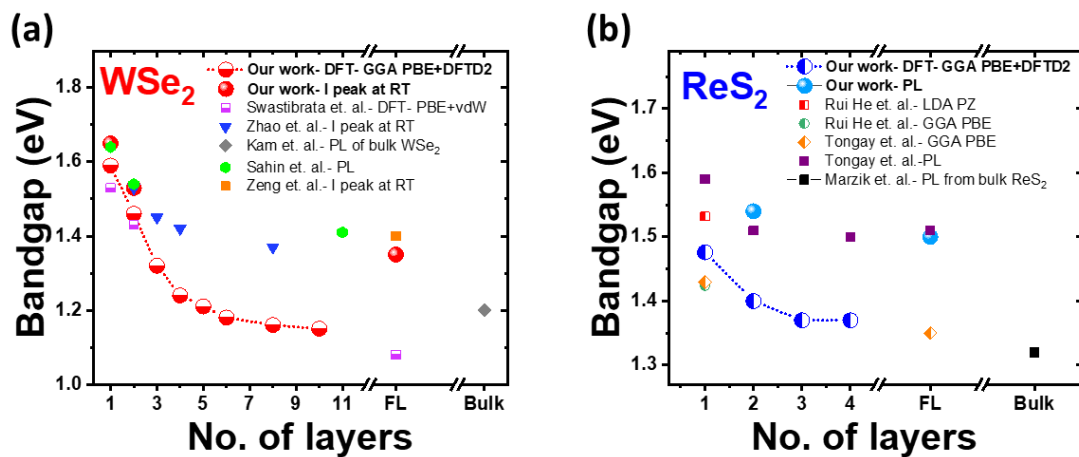


Figure S1.2: Comparison of calculated (DFT) and experimentally (PL) obtained bandgaps of (a) WSe₂ and (b) ReS₂ from this work and literature.

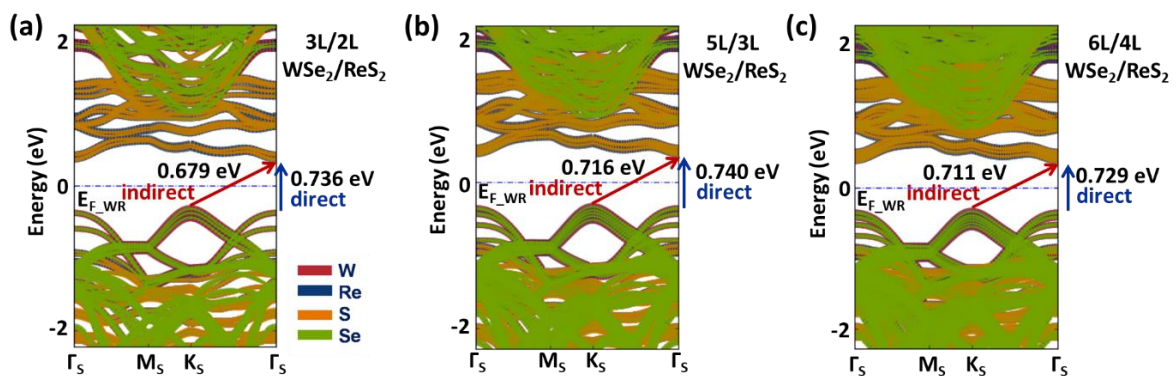


Figure S1.3: Projected bandstructures of various WSe₂/ReS₂ vdW heterostructures showing element-wise contributions. E_{F,WR} denotes the Fermi level position. The geometry optimized lattice constants and mean absolute strain values for various FL heterostructures were a= b= 6.61 Å and 0.66 % for 3L/2L WSe₂/ReS₂, a= b= 6.61 Å and 0.62 % for 5L/3L WSe₂/ReS₂, and a= b= 6.61 Å and 0.67 % for 6L/4L WSe₂/ReS₂.

S2: Optical microscope image of FL/FL WSe₂/ReS₂ heterostructure

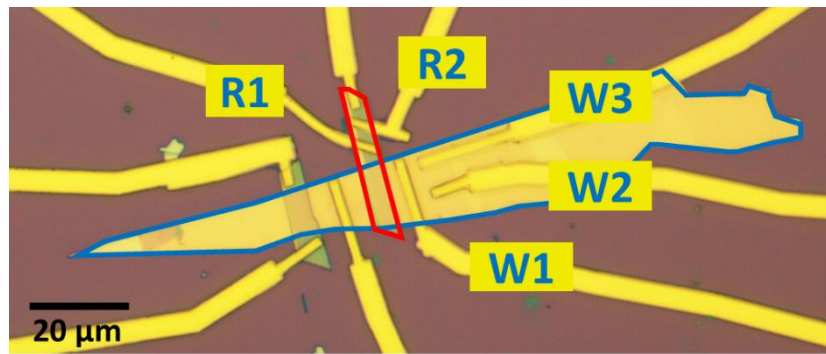


Figure S2: Optical microscope image of the FL/FL WSe₂/ReS₂ heterostructure presented in Figure 2. The WSe₂ flake is marked in blue and the ReS₂ flake in red.

Field effect transistors (FET) characteristics were studied for WSe₂ using the contacts W2 and W3 and for ReS₂ using the contacts R1 and R2. The diode characteristics were measured across the contacts R1 and W1.

S3: AFM images of WSe₂/ReS₂ heterostructures

AFM images and linescans of heterostructures of different thicknesses. The thickness values for the WSe₂ and ReS₂ are consistent with literature.^{14,15}

1. FL/FL WSe₂/ReS₂ heterostructure: A second FL/FL device besides the one reported in the main manuscript (Figure 2)

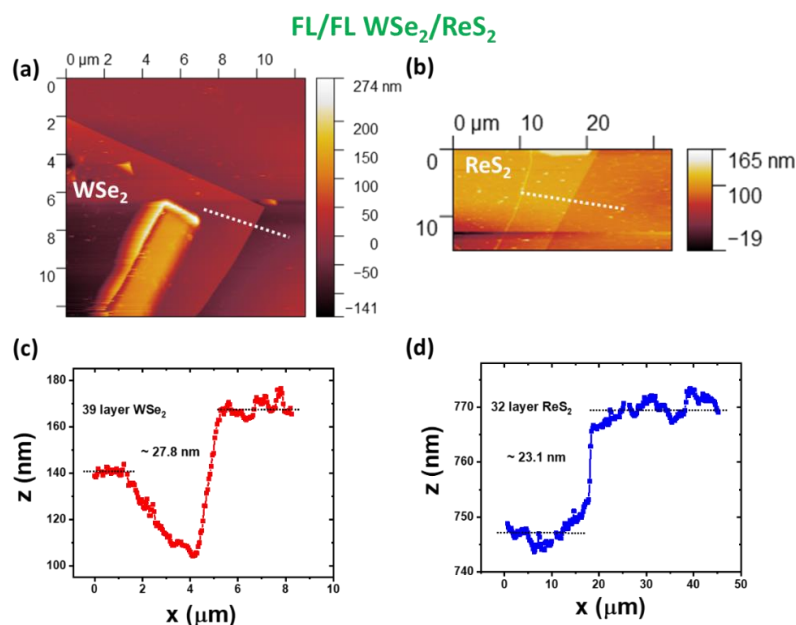


Figure S3.1: AFM images of (a) FL WSe₂ and (b) FL ReS₂ and the corresponding (c,d) linescans showing the thickness of the flakes.

2. FL/8L WSe₂/ReS₂ heterostructure: 65L/8L

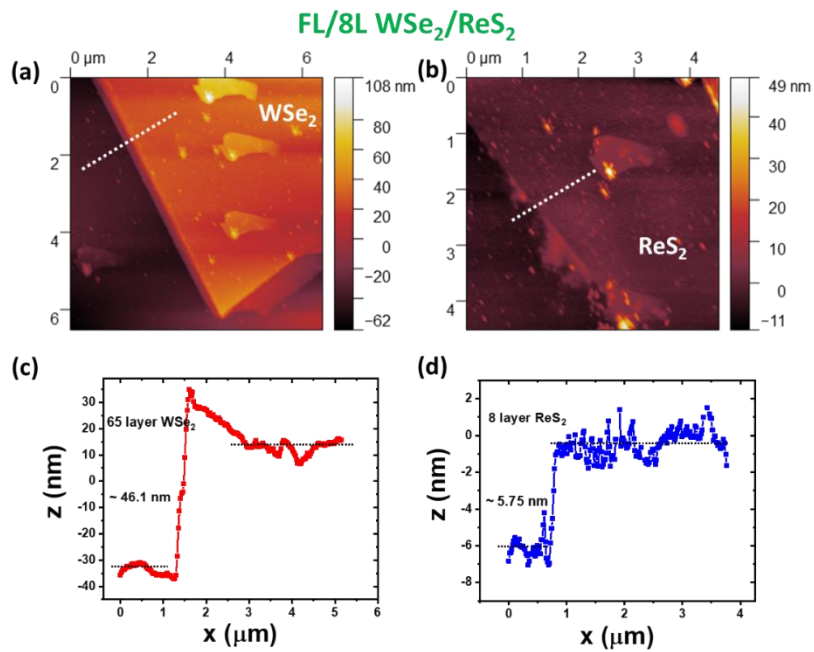


Figure S3.2: AFM images of (a) FL WSe₂ and (b) 8L ReS₂ and the corresponding (c,d) linescans showing the thickness of the flakes.

3. 2L/2L WSe₂/ReS₂ heterostructure

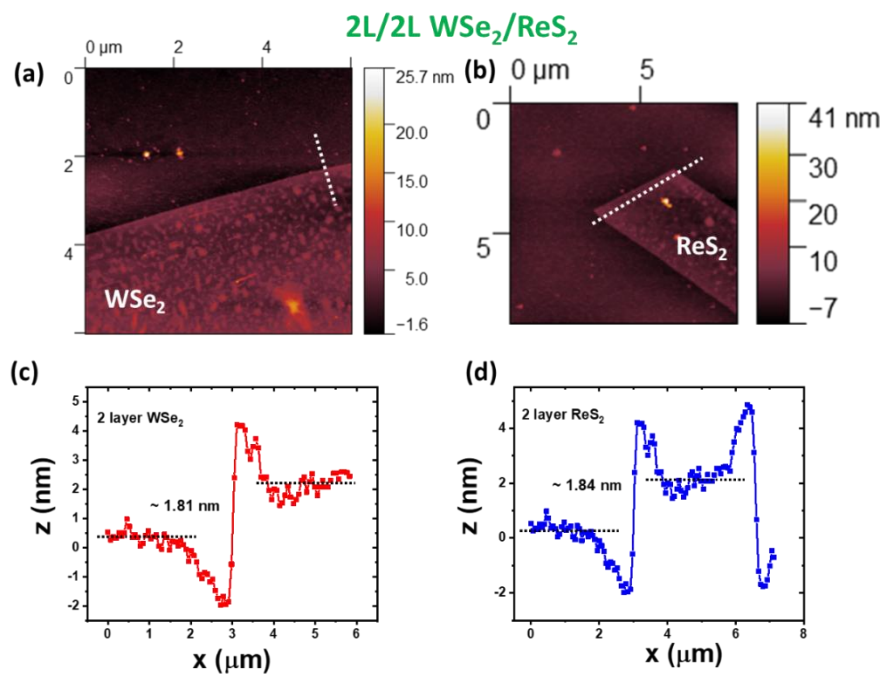


Figure S3.3: AFM images of (a) 2L WSe₂ and (b) 2L ReS₂ and the corresponding (c,d) linescans showing the thickness of the flakes

4. S4: Photoluminescence studies on WSe₂/ReS₂ heterostructures

Room temperature and low-temperature photoluminescence characterization was carried out to study the optical properties of the heterointerface. WSe₂/ReS₂ heterostructures with three distinct thickness configurations were considered:

1. Thick WSe₂ (65 layers)/ Thin ReS₂ (8 layers) → **FL/8L WSe₂/ReS₂**
2. Thin WSe₂ (2 layers)/ Thin ReS₂ (2 layers) → **2L/2L WSe₂/ReS₂**
3. Thick WSe₂ (32 layers)/ Thick ReS₂ (28 layers): Similar to the heterostructure described in the main manuscript → **FL/FL WSe₂/ReS₂**

The measured PL peak positions are as follows:

Temp (K)	65L WSe ₂		32L WSe ₂		2L WSe ₂		28L ReS ₂	8L ReS ₂	2L ReS ₂
	A	I	A	I	A	I	D	D	D
300	1.59	1.35	1.59	1.35	1.60	1.53	1.50	1.50	1.54
25					1.69	1.53			1.6

Where, A is the transition from K of conduction band to K of valence band of WSe₂, I is the transition from the conduction band minima between Γ and K to Γ of WSe₂. Further, the D peak is due to the direct bandgap transition at Γ of ReS₂.

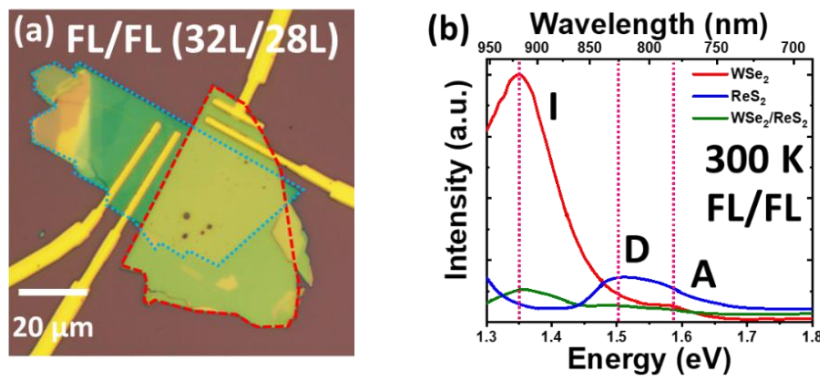


Figure S4: (a) Optical microscope image of FL/FL (32L/28L) WSe₂/ReS₂ heterostructure. (b) Room temperature PL peaks from individual materials and in WSe₂/ReS₂ heterostructure overlap region. There is a significant quenching of PL in the overlap region.

S5: Transfer characteristics of individual WSe₂ and ReS₂ FETs

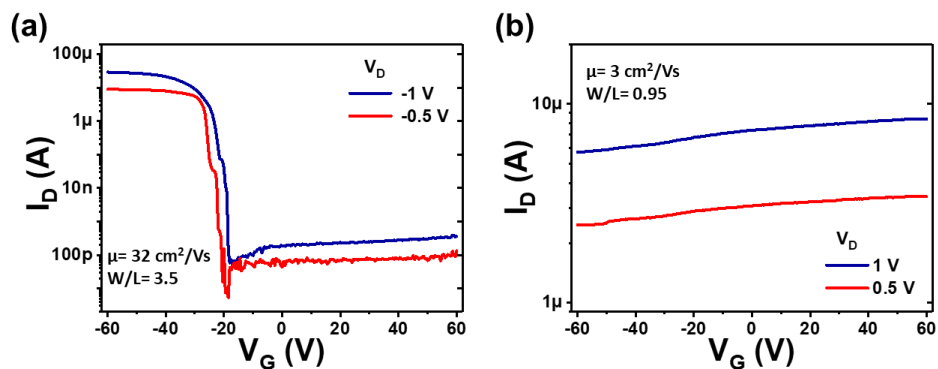


Figure S5.1: Transfer characteristics of (a) FL WSe₂ and (b) FL ReS₂.

Clear p- and n-type transport is observed in WSe₂ and ReS₂, respectively. The values of mobility (μ) and W/L are also marked.

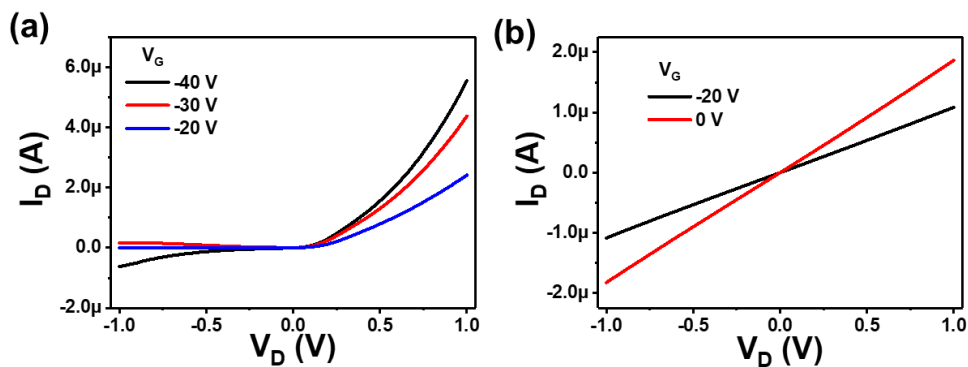


Figure S5.2: Output characteristics of (a) FL WSe₂ and (b) FL ReS₂.

The WSe₂ FET shows Schottky barrier dominated current transport. The ReS₂ FET displays ohmic characteristics.

S6: High on/off ratio in thin ReS₂ FET

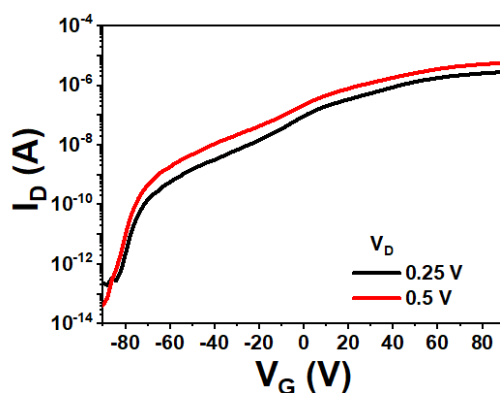


Figure S6: Transfer characteristics of thin ReS₂ FET.

In contrast to the transfer characteristics of the relatively thicker ReS₂ FET shown in Figure S5.1 (a), the transfer characteristics of trilayer ReS₂ (in S6) exhibits good modulation of the drain current with gate voltage. The current on/off ratio is 10⁸.

S7: Pt contacts: without Cr adhesion layer

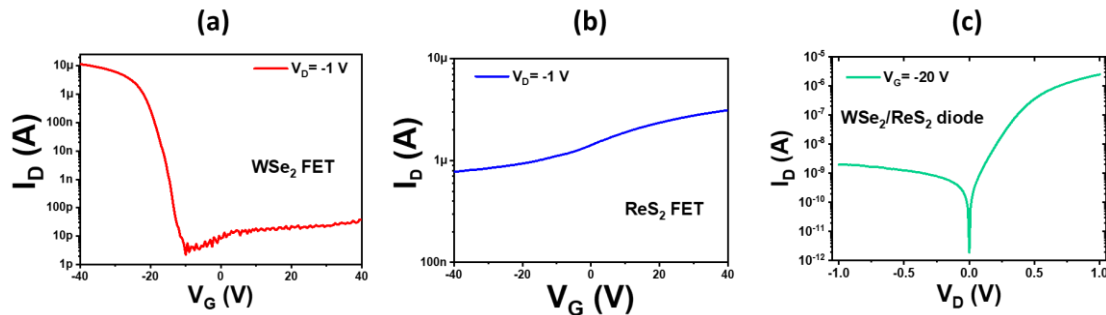


Figure S7: Transfer characteristics of (a) WSe₂ and (b) ReS₂ FET with Pt (50 nm)/Au (50 nm) contact. (c) I-V characteristics of the FL/FL WSe₂/ReS₂ heterojunction diode.

Pt is the choice of contact metal for our study. However, < 5 nm Cr is used as an adhesion layer to improve the sticking of Pt on Si/SiO₂ substrate. The use of such thin layers of Cr or Ti has been frequently employed during sputtering to improve the adhesion of metals like Au and Pt on Si/SiO₂ substrate. The transfer characteristics for the heterostructures without the thin Cr layer (above) are similar to those in Figure S5.

S8: Gate tunable I-V characteristics of a FL/FL WSe₂/ReS₂ diode with a maximum rectification ratio of 10⁵

I-V characteristics of a similar FL/FL WSe₂/ReS₂ heterostructure are shown in (a). Gate tunable rectification ratio and ideality factor are plotted in (b). The maximum rectification obtained is 10⁵ for $V_G = -20$ V. The ideality factor is ~ 2 and the current transport is recombination dominated.

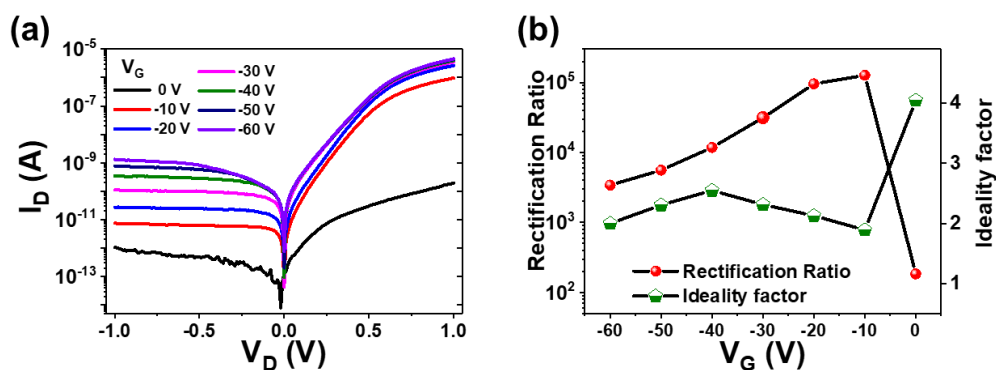


Figure S8: Gate-tunable (a) I-V characteristics and (b) rectification ratio and ideality factor of a similar FL/FL WSe₂/ReS₂ heterojunction diode.

When forward biased, a positive voltage is applied to WSe₂ and ReS₂ is kept grounded. Now, as described in Figure S10.2, for $V_G = -40$ V, there is an accumulation of majority charge carriers- electrons from ReS₂ and holes from WSe₂ at the heterointerface which can undergo interlayer recombination to yield a large current component, $I_{rec} \propto n_R p_W$, marked as region (1) in Figure S10.1 (n_R and p_W both being large). Additionally, the transport of majority electrons (holes) from the conduction (valence) band of ReS₂ (WSe₂) to the conduction (valence) band of WSe₂ (ReS₂) contribute to the over-the-barrier current (I_{maj}), which is less pronounced compared to I_{rec} . It should be noted that V_{Th} of the WSe₂ FET and of the p-branch of the forward bias transfer characteristic of the diode are similar. I_D shows an exponential decay marked by region (2) in Figure S10.1, which corresponds to a sub-threshold current ($I_D \propto \exp\left(\frac{q(V_G - V_{Th})}{k_B T}\right)$) due to transport dominated by WSe₂.

Thereafter, for $V_G > V_{Th}$ of WSe₂, region (3) shows an increasing current due to contribution from ReS₂. A polynomial function of the nature $I_D \propto A + B_1 x + B_2 x^2$ can be employed to fit the curve in region (3); the fit parameters are similar to those for the transfer characteristic of the ReS₂ FET. Finally, region (4) shows a nearly constant current defined by interlayer recombination, the magnitude diminished with respect to negative V_G owing to the reduced p_W , since WSe₂ is now in the off state. The inset in Figure S10.1 shows the variation of $n_R p_W$ based on calculated carrier densities and shows good resemblance with the forward bias diode transfer curve.

For the reverse bias case in Figures S10.2 a(iii) and b(vi), since the direction of the source-drain electric field (E_D) is now reversed, the current is due to generation of charge carriers in WSe₂ (intralayer) or across the heterojunction (interlayer). The generation current (I_{gen}) takes the form, $I_{gen} \propto \gamma(V_G) G t_{eff}$. Here, γ is the charge carrier extraction efficiency which depends on V_G of the gated diode. G is the generation rate and t_{eff} is a V_D dependent length scale over which the generation processes take place. In addition to the electrostatic modulation of n_R and p_W , V_G also determines the effective barrier for the transport of electrons and holes across the heterojunction. Unlike n_R , p_W shows good tunability with V_G . Hence the dependence of γ on p_W is evident. The difference in reverse bias I_D between regions (5) and (6) in Figure 3d is due to the change in γ . The magnitude of γ is much larger for negative V_G due to significantly larger p_W in WSe₂ at negative gate biases.

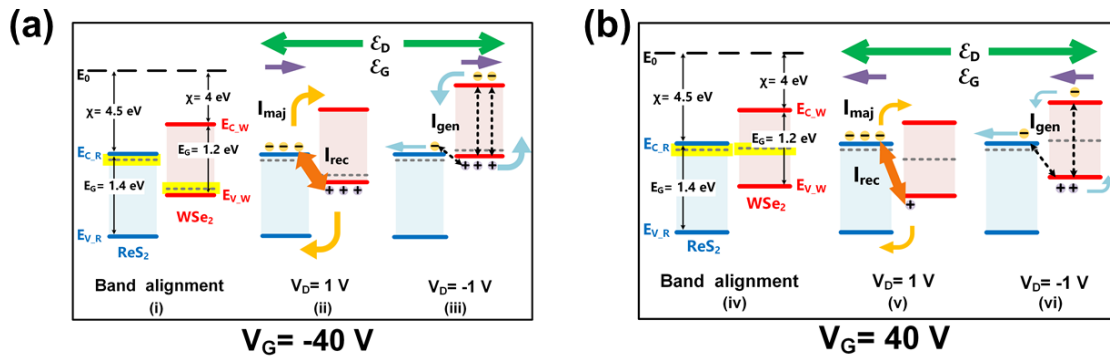


Figure S10.2: (a) Energy band diagrams for $V_G = -40$ V: (i) band alignment in WSe₂ and ReS₂ with their respective Fermi levels defined by the gate voltage, (ii) under forward bias, the dominant charge transport is governed by interlayer recombination of the majority carriers giving rise to I_{rec} , and (iii) for reverse bias the reduced current is due to intralayer and interlayer generation denoted by I_{gen} . (b) At $V_G = 40$ V, (iv) shows band alignment with the position of the Fermi levels, (v) under forward bias, I_{rec} is lower than the $V_G = -40$ V case due to lower p_W , and (vi) under reverse bias, a reduced (V_G) results in lower I_{gen} . E_G and E_D are the electric fields due to back gate and source-drain bias, respectively. The relative thickness of the arrows indicates the magnitude of the currents.

S11: Photocurrent in thinner (FL/8L and 2L/2L) heterostructures

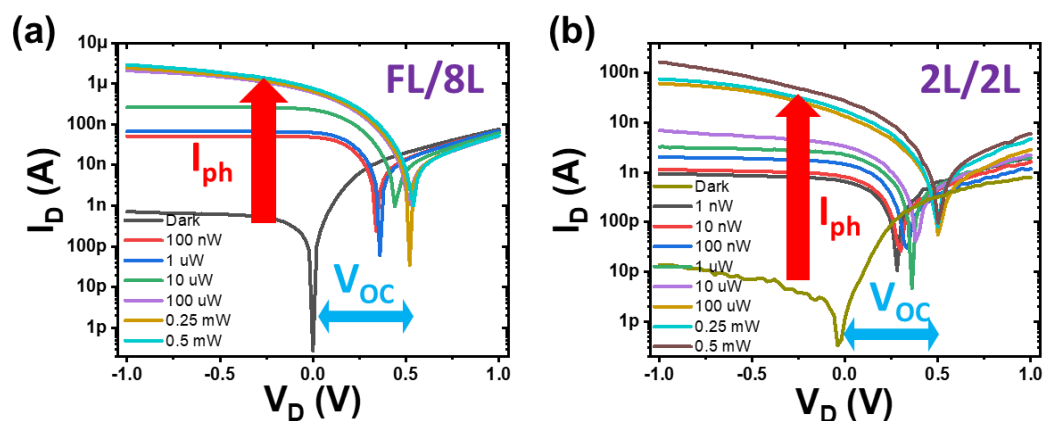


Figure S11: The I-V characteristics under 532 nm focused laser illumination are shown for (a) FL/8L and (b) 2L/2L heterostructure diodes. Photocurrent generation and V_{oc} are highlighted.

The photocurrent is lower for the heterostructures composed of thinner flakes owing to the lower absorption of incident radiation and thereby, reduced generation of electron-hole pairs.

S12: Absorption spectrum of thick ReS₂ flake

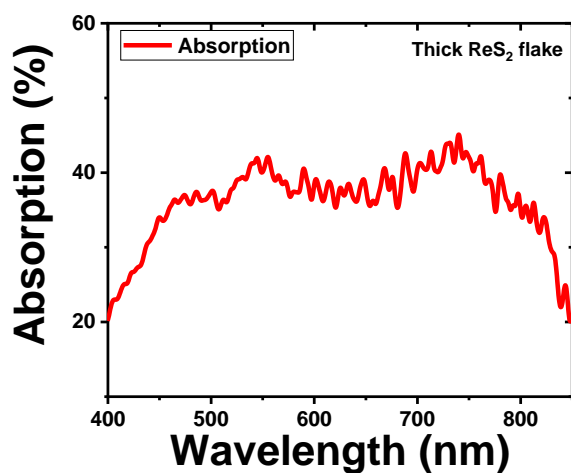


Figure S12: Absorption spectrum of thick ReS₂ flake on sapphire substrate measured for small angle of incidence (15°) shows high optical absorption.

S13: Reverse bias transfer characteristics under illumination for negative V_G (FL/FL structure)

The generation current under reverse bias (Figure S12a) can be described as, $I_{gen} \propto \gamma(V_G)G_L t_{eff}$, where G_L is the photogeneration rate due to the incident radiation. The dependence on γ (hence, V_G) is the same for illuminated and dark characteristics since illumination does not change the dependence of p_w on V_G that determines γ . Electric field due to the gate bias (E_G) at the vertical overlap region is parallel to E_D for negative V_G and is in the opposite direction for positive V_G (Figure S12b). Hence, for negative V_G , the gate-induced and the photogenerated electrons (holes) in ReS_2 (WSe_2) are both directed towards the contacts which leads to a larger net current compared to positive V_G . For $V_G < -20$ V, this enhanced field-assisted transport of the photogenerated minority carriers across the heterojunction is shown by the thicker blue arrows in Figure S12b. In contrast, for positive V_G , the net electric field that drives the photogenerated minority carriers is diminished.

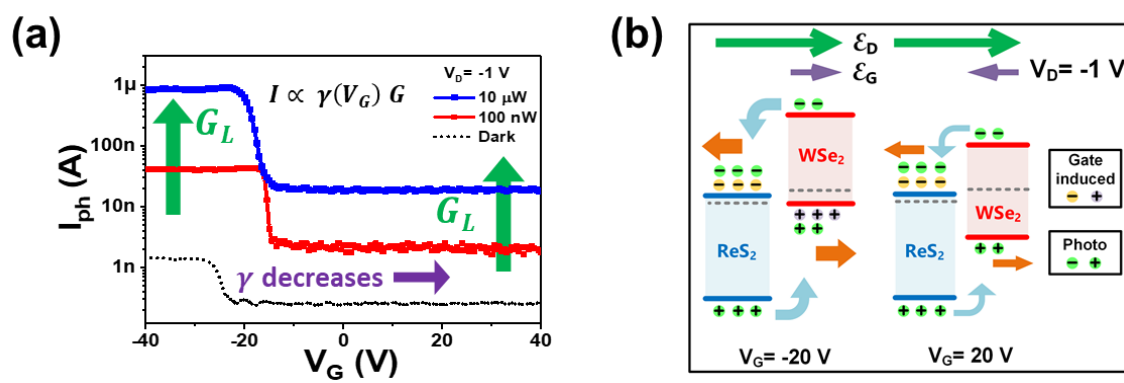


Figure S13: (a) Transfer characteristics of FL/FL WSe_2/ReS_2 heterostructure diode under reverse bias at 100 nW and 10 μ W incident laser illumination. The dark characteristics are shown in dotted lines. (b) Representative band diagrams depicting the band alignments under reverse bias for $V_G = \pm 20$ V.

S14: Transfer characteristics under illumination for forward bias ($V_D = 1$ V) (FL/FL structure)

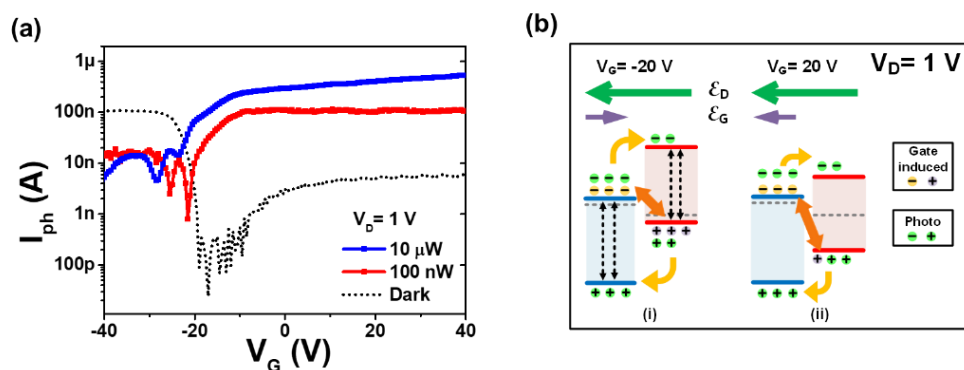


Figure S14: (a) Transfer characteristics of FL/FL WSe_2/ReS_2 heterostructure under forward bias at 100 nW and 10 μ W incident laser illumination. The dark characteristics are shown in dotted lines. (b) Representative band diagrams depicting the band alignments under forward bias for $V_G = \pm 20$ V.

Dependence of the photocurrent on the gate voltage is shown in (a) and representative forward bias band diagrams at $V_G = -20$ V and $V_G = 20$ V are described in (b). A constant generation rate independent

of the gate voltage is considered. The carriers induced due to the gate voltage as well as the photogenerated carriers are marked in (b). For $V_G < -20$ V, the increased number of carriers leads to enhanced recombination thereby lowering the photocurrent as compared to $V_G > -20$ V. Also, the electric field due to the source-drain bias is in the direction of the gate field for positive V_G .

S15: Ideality factor of the WSe₂/ReS₂ photovoltaic device

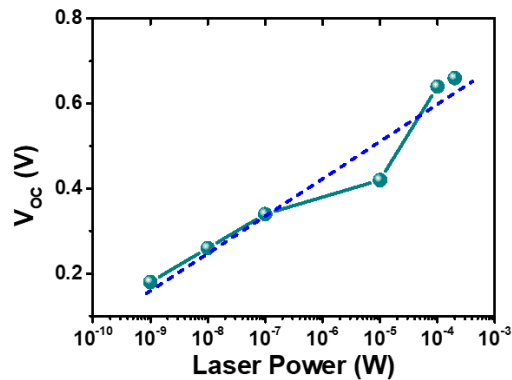


Figure S15: V_{OC} vs. incident laser power for the FL/FL heterostructure. The ideality factor of the photovoltaic device is obtained from the slope of the curve.

From the Shockley diode equation for a photovoltaic cell, the ideality factor (n_{id}) can be determined under open circuit conditions by:

$$\frac{\partial V_{OC}}{\partial \ln P_{laser}} = n_{id} \frac{k_B T}{q} \quad (1)$$

A $n_{id} = 1.5$ is obtained, implying both Langevin (direct recombination) and SRH (trap assisted recombination mechanisms) influence the current transport.

S16: V_{OC} dependence on gate voltage for FL/FL heterostructure

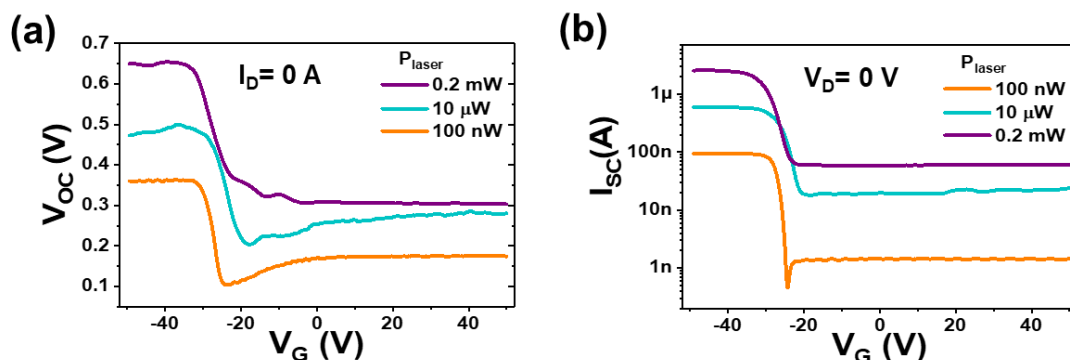


Figure S16: Gate voltage dependence of (a) V_{OC} and (b) I_{SC} at different illumination powers.

S17: V_{OC} dependence on flake thickness

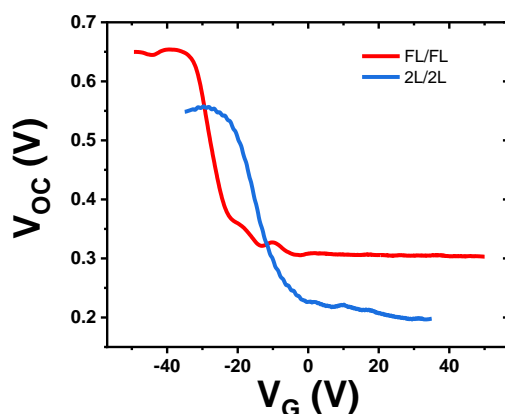


Figure S17: Gate voltage dependence of V_{OC} for heterostructures of different thicknesses (FL/FL and 2L/2L).

The open circuit voltage depends on the dark current as well as the current under illumination. Since the photocurrent is higher for the FL/FL heterostructure, the V_{OC} values are higher. However, the dependence of the V_{OC} with back gate voltage is similar for both devices.

References:

- (1) QuantumATK version 2018.06, Synopsys Quantumwise A.
- (2) Perdew, J. P.; Burke, K.; Ernzerhof, M. Generalized Gradient Approximation Made Simple. *Phys. Rev. Lett.* **1996**, *77* (18), 3865–3868. [https://doi.org/DOI 10.1103/PhysRevLett.77.3865](https://doi.org/DOI%2010.1103/PhysRevLett.77.3865).
- (3) Ozaki, T. Variationally Optimized Atomic Orbitals for Large-Scale Electronic Structures. *Phys. Rev. B* **2003**, *67* (15), 155108. <https://doi.org/10.1103/PhysRevB.67.155108>.
- (4) Ozaki, T.; Kino, H. Numerical Atomic Basis Orbitals from H to Kr. *Phys. Rev. B* **2004**, *69* (19), 195113. <https://doi.org/10.1103/PhysRevB.69.195113>.
- (5) Grimme, S. Semiempirical GGA-Type Density Functional Constructed with a Long-Range Dispersion Correction. *J. Comput. Chem.* **2006**, *27* (15), 1787–1799. <https://doi.org/10.1002/jcc.20495>.
- (6) Persson, K. Materials Data on ReS_2 (SG:2) by Materials Project. 2014. Materials Data on ReS_2 (SG:2) by Materials Project. 2014.
- (7) Dann, T. E.; Tiong, K. K.; Chen, J. L.; Huang, Y. S.; Ho, C. H. Electronic Structure of ReS_2 and ReSe_2 from First-Principles Calculations, Photoelectron Spectroscopy, and Electrolyte Electroreflectance. *Phys. Rev. B* **2002**, *60* (23), 766–771. <https://doi.org/10.1103/physrevb.60.15766>.
- (8) Bhattacharyya, S.; Singh, A. K. Semiconductor-Metal Transition in Semiconducting Bilayer Sheets of Transition-Metal Dichalcogenides. *Phys. Rev. B - Condens. Matter Mater. Phys.* **2012**, *86* (7), 1–7. <https://doi.org/10.1103/PhysRevB.86.075454>.
- (9) Kam, K. K.; Parkinson, B. A. Detailed Photocurrent Spectroscopy of the Semiconducting Group VIB Transition Metal Dichalcogenides. *J. Phys. Chem.* **1982**, *86* (4), 463–467. <https://doi.org/10.1021/j100393a010>.

- (10) Zhao, W. J.; Ribeiro, R. M.; Toh, M. L.; Carvalho, A.; Kloc, C.; Neto, A. H. C.; Eda, G. Origin of Indirect Optical Transitions in Few-Layer MoS₂, WS₂, and WSe₂. *Nano Lett* **2013**, *13* (11), 5627–5634. <https://doi.org/10.1021/nl403270k>.
- (11) Schutte, W. J.; Deboer, J. L.; Jellinek, F. Crystal-Structures of Tungsten Disulfide and Diselenide. *J. Solid State Chem.* **1987**, *70* (2), 207–209. [https://doi.org/Doi.10.1016/0022-4596\(87\)90057-0](https://doi.org/Doi.10.1016/0022-4596(87)90057-0).
- (12) He, R.; Yan, J. A.; Yin, Z.; Ye, Z.; Ye, G.; Cheng, J.; Li, J.; Lui, C. H. Coupling and Stacking Order of ReS₂ Atomic Layers Revealed by Ultralow-Frequency Raman Spectroscopy. *Nano Lett* **2016**, *16* (2), 1404–1409. <https://doi.org/10.1021/acs.nanolett.5b04925>.
- (13) Marzik, J. V; Kershaw, R.; Dwight, K.; Wold, A. Photoelectronic Properties of ReS₂ and ReSe₂ Single-Crystals. *J. Solid State Chem.* **1984**, *51* (2), 170–175. [https://doi.org/Doi.10.1016/0022-4596\(84\)90330-X](https://doi.org/Doi.10.1016/0022-4596(84)90330-X).
- (14) Tongay, S.; Sahin, H.; Ko, C.; Luce, A.; Fan, W.; Liu, K.; Zhou, J.; Huang, Y.-S.; Ho, C.-H.; Yan, J.; et al. Monolayer Behaviour in Bulk ReS₂ Due to Electronic and Vibrational Decoupling. *Nat. Commun.* **2014**, *5*, 3252. <https://doi.org/10.1038/ncomms4252><https://www.nature.com/articles/ncomms4252#supplementary-information>.
- (15) Li, Y.; Li, X.; Yu, T.; Yang, G. Accurate Identifi Fi Cation of Layer Number for Few-Layer WS₂ and WSe₂ via Spectroscopic Study. **2018**.